Journal of Renewable Materials

Tech Science Press

DOI: 10.32604/jrm.2023.024772 Published Online: 20 October 2022

check for updates

REVIEW

Thermomechanical Energy Converters for Harvesting Thermal Energy: A Review

Oleg P. Dimitriev*

V. Lashkaryov Institute of Semiconductor Physics, NAS of Ukraine, Kyiv, 03028, Ukraine

*Corresponding Author: Oleg P. Dimitriev. Email: dimitr@isp.kiev.ua

Received: 08 June 2022 Accepted: 02 August 2022

ABSTRACT

Thermal energy, i.e., the electromagnetic energy in the infrared range that originates from the direct solar radiation, outgoing terrestrial radiation, waste heat from combustion of fuels, heat-emitting electrical devices, decay of radioactive isotopes, organic putrefaction and fermentation, human body heat, and so on, constitutes a huge energy flux circulating on the earth surface. However, most energy converters designed for the conversion of electromagnetic energy into electricity, such as photovoltaic cells, are mainly focused on using a narrow part of the solar energy lying in the visible spectrum, while thermomechanical engines that are fueled by heat in the broad energy range and then convert it into mechanical work or store it as mechanical deformation, are paid less attention. Although the efficiency of thermomechanical devices is relatively low, they can be applied to collect waste heat which otherwise contributes to negative climate changes. In this review, operational principles of thermomechanical energy converters and a description of basic devices and materials that utilize thermal energy are given. In addition to conventional macroscopic engines, based on thermoacoustic, thermomagnetic, thermoelastic, hydride heat converters, and shape memory alloys, the emergent devices are described which are classified as smart actuators, breathing frameworks, thermoacoustic micro-transducers, nanomechanical resonators, plasmomechanical systems, and optothermal walkers. The performance of the different types of thermomechanical energy converters is described and compared.

KEYWORDS

Thermal energy; smart actuator; thermomechanical converter; thermoelastic engine; molecular machines; emergent devices

Abbreviations

AB	azobenzene
BMMPA	broadband metamaterial perfect absorber
C	chair
CNT	carbon nanotubes
DBCOD	dibenzocyclooctadiene
GNR	graphene nanoribbon
GO	graphene oxide
EC	ethylene cellulose
HTMH	high-temperature metal hydride
IR	infrared

LCE	liquid crystal elastomer
LCN	liquid crystal network
LTMH	low-temperature metal hydride
MOF	metal-organic framework
NTE	negative thermal expansion
NIR	near infrared
NP	nanoparticle
PCE	power conversion efficiency
PEO	poly(ethylene oxide)
PNIPAM	poly(N-isopropylacrylamide)
rGO	reduced graphene oxide
SMA	shape memory alloy
SME	shape memory effect
SMP	shape memory polymers
SMPC	shape memory polymer composite
SCO	spin crossover
STF	solar thermal fuel
ss-PCM	solid−solid phase-change material
SSPT	solid-to-solid phase transitions
SWCNT	single-wall carbon nanotube
TEG	thermoelectric generator
TMG	thermomagnetic generators
TB	twist-boat
UV	ultraviolet

1 Introduction

Low-grade thermal energy in the form of the waste heat produced by either industrial or natural processes constitutes an enormous energy reserve that remains currently almost unexploited. Thermal energy, whose electromagnetic spectrum covers a broad infrared (IR) range, can originate from different sources, such as direct solar radiation, outgoing terrestrial radiation, waste heat due to combustion of fuels, heat-emitting electrical and electronic devices, decay of radioactive isotopes, human body heat, heat from organic putrefaction and fermentation, etc.; these energy sources give rise to a huge energy flux circulating on the Earth surface. For example, almost half of the solar radiation reaching the earth surface belongs to the IR region and even a larger amount of IR energy is re-emitted from the earth surface in the form of terrestrial radiation of the planet, which is a black body with an average temperature of T_{Earth} = 288 K. The power of this thermal energy is huge and constitutes about $\sim 10^{17}$ W; i.e., this is comparable with the power of direct solar radiation. Furthermore, the total amount of waste heat constitutes up to 72% of all electrical energy produced in 2016 [1].

However, harvesting low-grade heat is a challenging issue because of the low Carnot efficiency. Different methods aimed at harvesting thermal energy, which can be conventionally divided into photonic (photoelectric) and thermal devices, suffer from low efficiency and other drawbacks as well. Photonic methods are based on electronic excitation as a result of absorption of the IR radiation, by picking up an electron from the ground state or valence band to the excited state or conduction band of molecules or crystals. Since the energy of IR photons is relatively low, less than 1.6 eV, narrow-gap materials are needed to harvest IR radiation. For this purpose, narrow-gap inorganic semiconductors and semimetals (such as $Hg_xCd_{1-x}Te$, Ge:Cu, Ge:Zn, Si:As, etc.), inorganic quantum wells and quantum dots,

superlattices, and some organic compounds can be employed [2]. However, the energy of electronic excitations in the low-energy IR range is comparable to the thermal energy at room temperature (~26 meV); therefore, the vibrational excitations affect the operation of such photonic devices and relevant efforts should be undertaken to reduce the thermal noise by cooling the absorber. The longer the wavelength of the IR absorption, the deeper the cooling temperature should be. Although the peak quantum efficiency of the best photoelectric converters exceeds 80% [3], the required low-operation temperatures remain the greatest disadvantage of the photonic systems for harvesting thermal energy, since these systems require additional energy for cooling too. Also, the power conversion efficiency (PCE) of photonic devices in the IR is low. For example, the best IR photovoltaic cells based on colloidal quantum dots demonstrate PCE of 4.2% [4].

Thermal engines usually operate owing to the available temperature gradients and/or heat flows. For example, the temperature gradient in thermoelectric generators (TEGs) leads to the diffusion of charge carriers, where the different mobility of electrons and holes gives rise to the net flow of charged carriers between the hot and cold sides of the device, which in turn creates a voltage difference. The typical efficiency of TEGs is around 5%–8% [5]. The other drawback of materials used in both photonic and thermal devices that convert electromagnetic energy to electricity is their cost, which is rather high.

On the other hand, thermomechanical energy converters that can be used for conversion of thermal energy directly into mechanical work or store it as mechanical deformation are paid less attention. Although efficiency of such thermomechanical devices is relatively low, their cost is relatively cheap and they can be applied to collect waste heat that otherwise contributes to the negative climate changes. Therefore, these can be used as a reasonable alternative to photonic and thermal devices which convert thermal energy to electricity.

This review just appeals to the above type of devices as relatively cheap and simple devices which can be made of renewable materials as well and which can operate in the low-energy domain where conventional solar cells are silent. In this review, operational principles of thermomechanical energy converters and description of basic devices and materials that are fed by thermal energy are collected. After a brief overview of traditional thermomechanical devices which include thermoacoustic, thermomagnetic, thermoelastic, shape memory alloy, and hydride heat converters, description of emergent devices, such as smart actuators, breathing frameworks, thermoacoustic transducers, nanomechanical resonators, plasmomechanical systems and optothermal walkers are given. Performance of the different types of thermomechanical energy converters is discussed and compared as well.

2 Trends in Development of Thermomechanical Energy Converters

Development of thermomechanical actuators for harvesting thermal energy during the last decades follows a two-fold trend (Fig. 1). The first trend corresponds to the miniaturization of the thermomechanical actuators from macro- to micro- and nano-scale, i.e., the trend to manufacture ever smaller mechanical products and devices. Although the miniaturization of a device in some cases can be accompanied by worsening its performance due to the loss of coupling efficiency at small scales, complex manufacturing processes, and increasing power consumption [6], overall, this trend looks reasonable for this field, as specific operation of thermomechanical energy converters occurs due to conversion of thermal energy into mechanical one; therefore, they do not require wires or batteries, electrical or chemical stimuli for their mechanical mobility, which could otherwise restrict this trend. This trend offers exciting perspective of development of emergent fields such as (i) health control where nano-actuators can be deployed inside the human body and self-controlled either by body temperature or remotely controlled over the Internet by an external user such as a healthcare provider [7]; (ii) design of nano-scale robotics and nanotools able, for example, to manipulate with nano-objects (nanotubes, bio-nanoparticles, etc.) by using nanotweezers, such as bimetallic composites based on Ti_2NiCu alloy with

shape memory effect [8,9]; (iii) surface nano-patterning in the form of the surface relief grating by photo-isomerization of azopolymer being on the surface of some nano-objects such as microspheres, wires, or thin films at temperatures well below the glass transition temperature of the azopolymer [10]; (iv) design of nano-sensory devices able for the ultrasensitive detection of zeptogram masses [11], nanoscale temperature mapping [12] or nano-antenna radiation detecting [13] with a resolution exceeding the diffraction limit. In this direction, a complete understanding of the mechanical behavior of nano-actuators is crucial for the design of nanodevices and nanosystems. Therefore, the flexural, stability and vibration analysis of various nano-actuators in the form of nanobeams, nanoplates, nanowires, nanotubes, graphene sheets and nanoshells, etc., has received a great attention in the recent years [14].

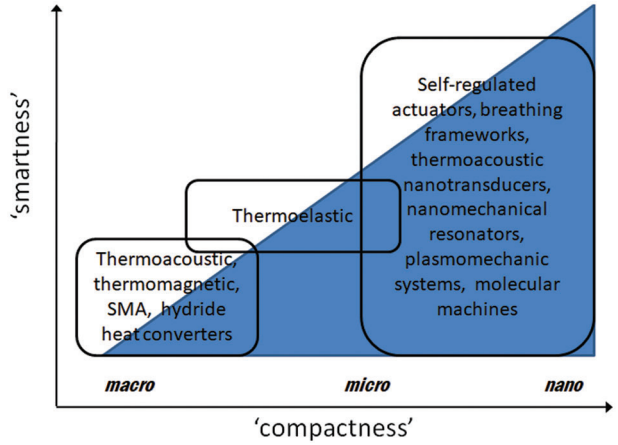

Figure 1: Overview of the different groups of thermomechanical devices in terms of a two-dimensional scheme of their development trends

The second trend in development of thermomechanical energy converters is the use of smart, programmable, self-regulated actuators able to mimic natural processes. For example, one of the most ambitious challenges is the creation of smart soft robotics with the design of actuators closely resembling the skeletal muscle actuation system and capable of reaching performances comparable to the skeletal muscles [15]. Smart actuators are usually manipulated by a feedback control, communication capabilities, position control, and fault detection, which can be achieved by application of multiple or qualitatively different stimuli (such as light, heat, electricity, magnetism, humidity, pH, etc.), by programmable logic, and/or by integration of functionally different multiple segments in the same device [16]. For example, a flexible graphene-based Janus film composed of two components, a graphene oxide (GO) layer and a reduced GO (rGO) layer, can roll up on the short-side in response to moisture stimulation due to the hygroscopic expansion of the GO layer, while the film rolls up in the opposite direction under the thermal stimulation, which occurs due to the negative thermal expansion of the rGO layer [17]. In this way, the GO/rGO Janus film can be triggered by a sweaty or warm hand with an improved sensitive response capacity, demonstrating an intelligent actuating behavior. Also, smart actuators can integrate energy harvesters (which are thermomechanical engines themselves) and side transducers, or these can be self-powered by combining the cable-driven actuation with soft triboelectric nanogenerators, which makes them self-sustainable systems, which can be considered for implantable and wearable diagnostic, therapeutic and treatment applications as well [18,19].

Taking into account the above trends, the known thermomechanical actuators able for thermal energy conversion will be roughly divided into three groups (Fig. 1). The first group comprises conventional macroscopic devices whose construction and/or functioning requires a sizeable amount of material. These include thermoacoustic, thermomagnetic, hydride heat converters, and shape memory alloys. The other

group is related to emergent devices whose construction and/or operation principles are realized on the micro- or nano-scale. The driving forces in these devices are due to nanoscale processes such as molecular switch, change in interatomic distances, etc. This group of devices includes smart nano-actuators, breathing frameworks, thermoacoustic micro/nanotransducers, nanomechanical resonators, plasmomechanical systems, and molecular machines or nano-walkers. Finally, thermoelastic devices comprised of elastic materials such as polymers and elastomers can be referred to as a separate, intermediate group. These are usually hybrid devices that can integrate switchable molecules and a polymer matrix. The operation of these devices therefore can be based due to switches on the molecular level, but these also require a sizeable amount of material to realize their elastic properties. The above three groups of devices are reviewed in more detail below.

3 Conventional Thermomechanical Energy Converters

3.1 Thermoacoustic Heat Engines

A basic thermoacoustic heat engine converts heat into acoustic wave energy. The major elements of such a device are two heat exchangers near the closed end of a resonant tube, with a regenerator stack situated between them in the form of a porous material producing an acoustic wave as gas flows between the two exchangers due to the temperature gradient which causes the gas to periodically expand and contract (Fig. 2). These oscillations lead to the generation of acoustic waves escaping the open end of the tube; the mechanical waves can be further converted into electrical energy by using a transducer [20]. In terms of the produced cycles, the thermoacoustic engine operates similar to a standard heat engine, possessing a compression, heating, expansion, and cooling cycle [21]. Thermoacoustic engines can be designed either as travelling wave devices which are better described by the Stirling cycle [22,23], or as standing wave devices which correspond to the Brayton cycle [24]. In the Brayton cycle, gas heated from the hot side of engine experiences the expansion through the regenerator stack that promotes the volume of gas to expand to the cold side, which reduces the gas temperature. Then, the local cool temperature of the wall forces the gas to contract and to reduce its pressure, completing the cycle. This cycle produces a corresponding standing wave in the tube, where the acoustic wavelength is defined by the tube dimensions (Fig. 2). If necessary, the acoustic energy can be further converted to electricity using a diaphragm or piezoelectric transducer at the open end of the thermoacoustic tube.

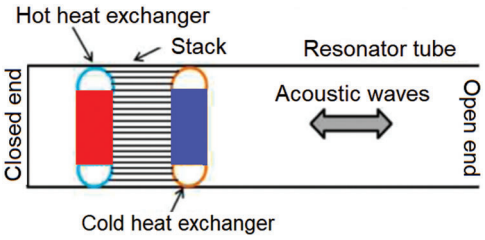

Figure 2: Scheme of a standing wave thermoacoustic heat engine

In the Stirling cycle, a travelling wave pressure is required, and the device must be tuned so that the energy is always added in phase with the input travelling wave, thereby amplifying the wave. The engine operates by moving the working fluid from the cold to the hot end, thus amplifying an acoustic pressure wave travelling from the cold to the hot side of the device. The increasing temperature of the gas, when flowing towards the hot end, causes the gas pressure to increase, followed by a pressure drop as the gas expands and flows back to the cool side.

The ideal Stirling cycle, being used in the traveling wave devices, is inherently more efficient than the ideal Brayton cycle that operates in the standing wave devices [24,25]. However, whereas in a standing wave stack deliberately imperfect thermal contact is sufficient, a travelling wave device requires narrower pores to

provide good thermal contact with the fluid, which gives rise to greater frictional losses, reducing practical efficiency. The most efficient Stirling-based device has performance near 40% of the Carnot limit, with a record reported efficiency being 49% of the Carnot limit (for the most efficient operating point corresponding to the drive ratio of 8.14% and engine temperature of 580°C), which corresponds to the neat PCE of 32% [25].

The advantage of the thermoacoustic engines is due to their environmental friendliness, potentially high reliability owing to simple structure and minimal number of moving parts, and reasonable efficiency. However, the need of large temperature gradients is their mere disadvantage. Application of modest temperature gradients on practice leads to low efficiency of such engines. For example, a temperature gradient of about 100 degrees by Celsius in a small-scale standing-wave thermoacoustic engine generates sound with the acoustic power of ∼100 mW and estimated thermoacoustic energy conversion efficiency of 5%–6% [26].

The reverse process, i.e., the conversion of mechanical energy into a thermal difference, can be also fulfilled, which is used in thermoacoustic refrigerators, where the gas adiabatically and alternatively compresses and expands, accompanied by the simultaneous change in gas pressure and temperature, where the pressure reaches a maximum or minimum along with corresponding changes in the temperature [27]. Application of the reverse process for gas liquefaction [28], medical storage with minimum reached temperature up to −19.7°C [29], etc., have been reported, which showed an exergy efficiency of 24% and cooling power of 2.1 kW achieved at 130 K [30].

3.2 Heat Engines Based on Shape Memory Materials

Materials that are able to recover their original shape after their deformation due to heating/cooling or by strain/stress are referred to as shape memory materials [31]. Historically, the shape memory property was first observed long time ago in metal alloys, such as gold–cadmium, copper–zinc, and nickel–titanium (NiTi) [32,33]; nevertheless, the shape memory alloy (SMA) materials have been receiving increasingly more attention and study in recent years as well. A SMA material possesses two different phases, i.e., austenite and martensite, between which a temperature-induced solid-state phase transition occurs, called also a martensitic phase transformation, which is accompanied by the shape memory effect (SME). The transformation between the conventional low-temperature and low-strength martensite phase and the high-temperature and high-strength austenite state usually occurs as a displacitive, lattice-distortive, first-order diffusionless athermal transformation, for example, the transformation from the high-temperature, body-centered cubic lattice austenitic phase to the low temperature, face-centered tetragonal lattice without atomic diffusion, which sometimes goes through an intermediate phase corresponding to a rhombohedral crystal structure in NiTi alloys that contain a surplus of nickel or nickel partly replaced with a third element [34]. Remembering a specific state of the alloy is achieved through forming and constraining the SMA in a desired shape and annealing it at a prescribed temperature, which represents a ‘training’ process. This process rearranges the dislocations present in the SMA in the way that allows the material to take on a new shape without internal stresses, which allows the SMA to be pliable at low temperatures [35]. The strain of the SMA material exhibits a hysteresis as a function of temperature, where the cycle begins from the martensite start temperature (Ms) to the martensite finish temperature (Mf), and the recovery, i.e., the reverse transformation that occurs on heating, beginning from the austenite start temperature (As), and ending at the austenite finish temperature (Af). Due to the hysteresis, some of the mechanical energy is lost in this process, and the austenite form generally possesses a higher strength than the martensite form [36].

Performance of SMA engines varies depending on their composition and construction features. Today, SMAs based on nickel–titanium (e.g., NiTi, NiTiCu, NiTiFe, etc.), iron (FePt, FeNiC, etc.), copper (CuSn, CuZn, etc.), silver (AgCd, etc.), gold (AuCd, etc.), and cobalt (CoNiAl, etc.) are commercially available, with the NiTi SMA to be the most popular and effective as it possesses better mechanical and

thermomechanical properties compared to the other SMAs such as iron or copper-based alloys [37]. Usually, SMA materials produce work density of the order of 10 J/g and have efficiency of several percents [38]. However, a record efficiency for a crankshaft Nitinol (NiTi) SMA heat engine has been recently reported, which produced the highest power output value of 4 watt, with 11.3% of engine efficiency [39].

Besides SMAs, shape memory polymers (SMPs) have been attracted increasing attention and research interest in the recent years [40–42]. SMPs have certain advantages before SMAs, due to their relatively high strain of 400%–800% (while SMAs reach only ~8%), easy and fast shape training, low cost, bio-compatibility and degradability, and because these can be processed at much lower temperatures and pressure and have higher efficiency compared to SMAs [43].

The entropic elasticity of polymers is the core mechanism of the SME in polymers [44]. The equilibrium entropy of an amorphous polymer phase is largely determined by chain-chain interactions, leading to strong coiled conformation of the polymer chain. Applied stress results in elongation of the random polymer coils along the stress direction; thereby, the number of chain-chain interactions becomes reduced, which also reduces the entropy [45]. A subsequent release of the stress causes the polymers to return back to their original coiled state with high entropy again. In this way, a "memory" about the polymer initial, undeformed state is persisted. But a long-time application of the stress (hours rather than seconds) can result in slippage of the polymer chains that yields irreversible non-elastic changes, which serves to erase the polymer "memory" concerning its original shape [46]. To prevent the slippage effect, SPMs are prepared by using interchain cross-linking, where chemical or physical cross-links fix the polymer in its most thermodynamically favorable shape, also called a permanent shape. However, in addition to cross-links, which restrain shape-fixing of the permanent shape and provide so-called "hard" regions, "soft" regions are also needed to facilitate transition of the polymer chains into a less coiled shape, called a temporary state [47]. The availability of the "soft" and "hard" regions of the polymer enables to lock and unlock its temporary shape. When a suitable trigger is applied, the cross-linking of the temporary shape is undone, resulting in "unfreezing" the polymer chains and allowing for a recovery of the permanent shape. The temporary shape can be generated by polymer training or programming [48], i.e., the process of shaping and fixing the polymer in its temporary shape via two processing steps (Fig. 3a). During the first processing step, the permanent shape is fixed by means of chemical or physical cross-linking. In the second step, the applied stress deforms the permanent shape into a temporary shape and, along with application of a suitable trigger assisting in "freezing" the shape-fixing regions, this leads to sustaining the temporary shape in the form of deformation. Therefore, when the stress is released, the polymer will maintain its temporary shape, while recovery of the permanent shape can be achieved by applying another trigger to the polymer to undo the cross-links introduced during the first step. Low and high temperatures can serve as corresponding triggers that provide the cycle of the polymer shape transformations (Fig. 3b).

In order to facilitate shape memory effect in SMPs induced by electromagnetic radiation, different fillers can be added to the polymer network, which results in formation of shape memory polymer composites (SMPCs) or shape memory hybrids. The fillers assist in absorption of heat, where different materials can be employed for that. For example, gold nanoparticles were used as fillers in poly(ethylene oxide) (PEO) [49] and poly(d,l-lactic acid) [50] networks, where the SME was actuated by the increase in temperature assisted by photothermal conversion of the Au particles. Silver nanoparticles grafted on cellulose nanocrystal were shown to promote a rapid IR response of the obtained SMPC [51]. Incorporation of the organic rare-earth complex, namely, $Yb(TTA)_3Phen$ and $Nd(TTA)_3Phen$, into poly[ethylene-*ran*-(vinyl acetate)] (PEVA) matrix yielded a selective photothermal conversion effect under the near-infrared (NIR) light at 980 and 808 nm, respectively [52]. Carbon-based materials that effectively transform light absorption into the heat, such as carbon nanotubes and carbon nanodots, were also used as SME triggers in different shape memory hybrids. Wu et al. synthesized polyvinyl alcohol–carbon dots composite which demonstrated SME under the ultraviolet (UV) light irradiation [53]. Polymer–carbon nanotube [54] and polymer–Fe_3O_4 nanoparticle

[55] thermo-responsive composites were shown to display SME under microwave radiation. By incorporating gold nanoparticle/reduced graphene oxide (AuNP-rGO) hybrids into the cross-linked poly(ε-caprolactone). Li et al. [56] showed a synergistic effect of AuNP-RGO on the light-actuated shape recovery speed of this SMPC. Natural sunlight-actuated SMPC with reversible shape change and self-healing abilities based on conductive polymer composite, i.e., chlorinated poly(propylene carbonate) filled with carbon nanotubes, was fabricated by Cui et al. [57]. The composite could lift 550 times their own weigh triggered by IR light and the shape recovery time of the composite triggered by natural sunlight was only 39 s. A novel SMP hybrid able to respond to both UV and NIR light and to make contraction and bending motions was demonstrated by Zhou et al. via loading $W_{18}O_{49}$ nanowires (NWs) modified by oligo(ethylene glycol) (OEG) into cross-linked polymer matrices of polyethylene glycol diacrylate (cPEGDA) [58]. The cPEGDA/$W_{18}O_{49}$ NW hybrid actuators exhibited stable helical deformation (right-handed and left-handed) by utilizing oriented chain segments of the crystalline polymer and vector sum of shape recovery forces. Qi et al. demonstrated shape memory triggered at body temperature (T_{trans} = 36.6°C) in bio-based Eucommia ulmoides gum/silica hybrids, which restored the permanent shape within 60 s at 37°C with a shape fixity ratio of 99% and shape recovery ratio near 100% [59]. However, the main drawback of SMPs remains their low mechanical strength and stiffness and also their recovery is accompanied by small forces. Therefore, among shape-memory materials, SMAs demonstrate the best performance today (Table 1).

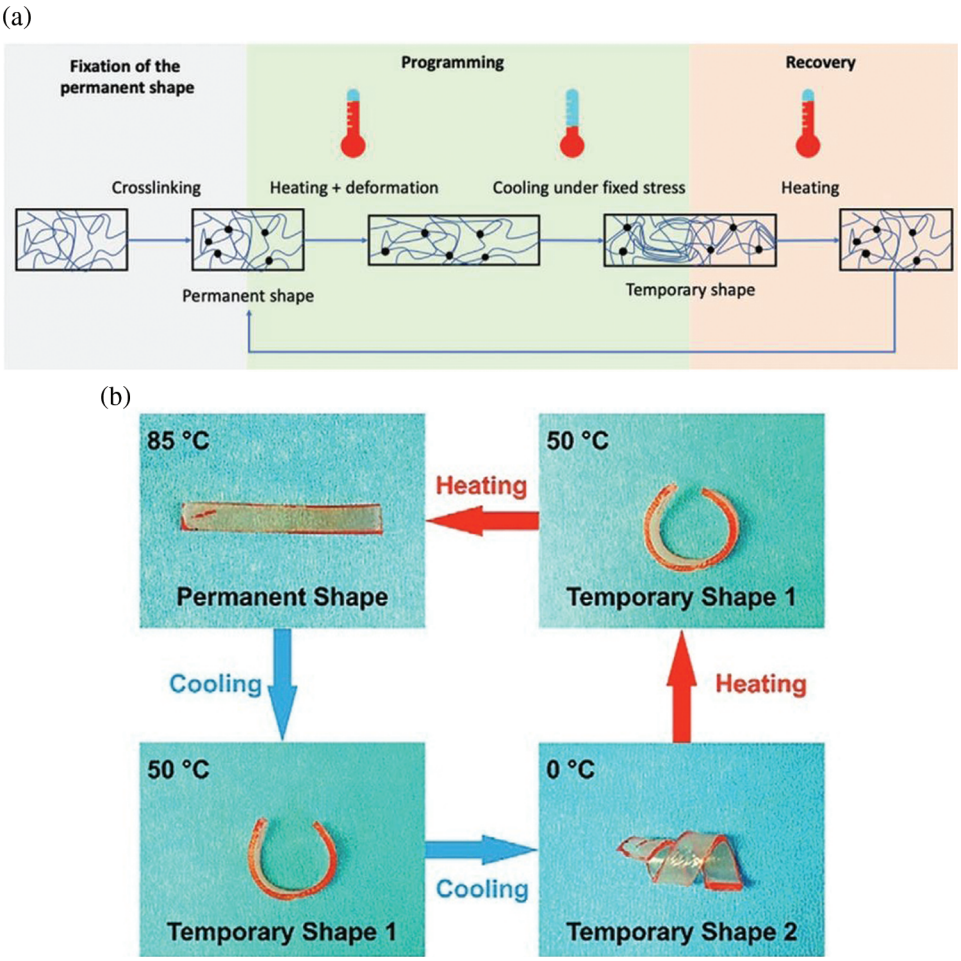

Figure 3: (a) Illustration of the thermally induced shape-memory effect via programming steps. Reprinted with permission from [60] Copyright 2020, John Wiley and Sons. (b) Reversible shape memory effect of polyolefin thermoplastic elastomer. Reprinted with permission from [61] Copyright 2019, American Chemical Society

Table 1: Performance of the different types of thermomechanical energy converters. For TMG, the temperature difference between hot and cold reservoirs is indicated

Energy converter type	Working material	Specific energy/work density	Output power/ power density	Efficiency, %	Ref.
Traveling-wave thermoacoustic engine	Helium gas		280 W	32	[25]
Standing-wave thermoacoustic engine	He-Ar mixture		200 W	11	[62]
SMA	NiTi	10 J/cm^3	30 W/cm^3	3	[43]
	NiTiCu	12 J/g		5.3	[63]
	Nitinol (NiTi)		4 W	11.3	[39]
TMG	La–Fe–Co–Si		118 μW/cm^3	$1.48 \cdot 10^{-4}$ ($\Delta T = 32$ K)	[64]
	Heusler alloy $Ni_{53.5}Mn_{23.8}Ga_{22.7}$		120 mW/cm^3	0.041 ($\Delta T = 3$ K)	[65]
	Gadolinium	600 μJ/g	200 μW/g	1–2 ($\Delta T = 60$ K)	[66]
Hydride heat engine	Mg-based	2.8 J/g		79	[67]
	Three-alloy hydride engine		80 mW/g	45	[68]
	$LaNi_5$		44 mW/g	35	[69]
Twisted nano-/ microfiber-based torsional and linear actuators	MWCNT/wax-coiled	1.36 J/g	27.9 W/g	<2	[70]
	Niobium NW/wax	48 mJ/cm^3	35 mW/g	<2	[71]
Breathing framework	Metastable *cis* AB isomer in $1 \supset AB_{1.0}$	28.9 J/g			[72]
Linear artificial muscle	Silicone-carbon fiber composite	10 μJ/g		0.005	[73]
	Liquid crystal elastomer	63 mJ/g	0.18 J/cm^3		[74]
	Nylon-6,6	2.48 J/g	27.1 W/g	<1	[75]
	Polyethylene	2.63 J/g	5.26 W/g	<1	[75]
Biological muscle*	Myofibers in a matrix of natural proteins	40 mJ/cm^3	50–284 mW/g	40	[37]

Note: *Biological muscle is given for comparison only; its operational principle is different from that of the thermomechanical engines.

3.3 Thermomagnetic Engines

Among various thermal energy harvesting devices available for capturing low-grade heat with temperature less than 100°C, the engines based on thermomagnetic effect can find niche applications. Thermomagnetic generators (TMGs) rely on the varying magnetization of a soft magnet that occurs upon change in its temperature. The magnet itself is being under applied magnetic field which renders a force to the magnet when it has nonzero magnetization available only at low temperature. In operation, a TMG alternately heats and cools the magnet by bringing it into contact with thermal reservoirs possessing

different temperatures. The resulting change in the magnetization is accompanied by a mechanical work performed by the magnetized material, or can produce currents in nearby conductive materials creating an electrical circuit, resulting in a net conversion of energy from thermal to electromagnetic (Fig. 4). Technically, design of TMGs is based on the use of ferromagnetic materials at temperatures close to the Curie point in order to facilitate the loss in material's magnetization upon heating. In this region, the internal magnetization of a magnet experiences large change at small temperature difference, causing high thermal-to-magnetic conversion efficiency.

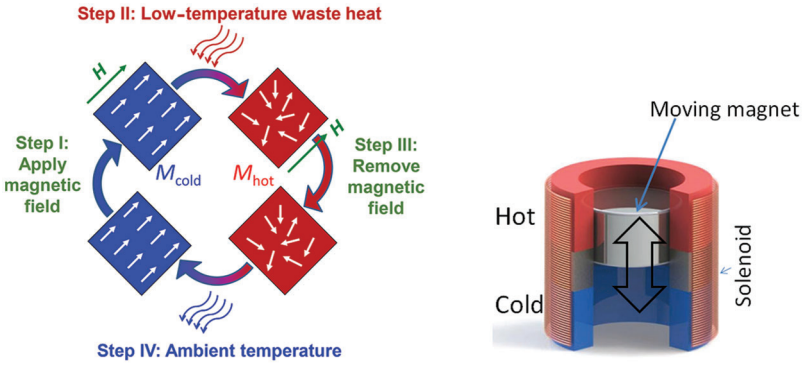

Figure 4: (a) Illustration of a thermomagnetic cycle and (b) basic design of a TMG using active magnet actuation. Part (a) reprinted with permission from [83] under Creative Commons Attribution (CC BY) license. Copyright 2021, Author(s)

Operation of TMGs can be realized via an active or passive mode. The movement between the hot and cold reservoirs in the passive mode occurs due to the change in the material magnetization. The movement to the hot reservoir is realized by magnetic force attraction between the magnet and the magnetic pole of the hot reservoir, whereas the restoring force between the magnet and the cold non-magnetic reservoir is realized by a spring or other means. Being in contact with the hot reservoir, the magnet is heated up and loses its magnetization; thus, the magnetic attraction decreases below the level of the restoring force. Under the force of the spring, the magnet returns to the cold reservoir. Being in contact with the cold reservoir, the magnet cools down; this is accompanied by the increase in its magnetization. That yields a strong enough magnetic force able to overcome the restoring force, resulting in movement of the magnet to the hot reservoir, completing the cycle [76].

In the active mode, instead of the magnetized hot reservoir an external force in the form of a cycling external magnetic field using electromagnets is applied to move the magnet between the reservoirs. That is, an external magnetic field is applied when cooling a magnet and increasing its magnetization, moving it to the hot reservoir; then the magnetic field is removed upon magnet heating [77]. The energy can then be harvested via induction.

The energy harvesting by TMG can be evaluated as thermodynamic efficiency which is defined as a fraction of usable output energy *vs.* thermal input energy Q_{in} during each cycle, where the upper limit of the output energy for the TMG is the magnetic energy E_m. The TMG efficiency is then given according to the formula

$$\eta = \frac{E_m}{Q_{in}} = \frac{\mu_0 \Delta M H}{Q_{in}} \tag{1}$$

where μ_0 is the magnetic field constant, M the magnetization and H the magnetic field.

In the early works, the theoretical limit for the TMG efficiency was evaluated to be below 1% [78]. However, recent efforts demonstrated that the gadolinium based TMGs can exhibit efficiency as high as 20.5% of the Carnot efficiency for the near room temperature operating condition with a temperature gradient of only 5 K and magnetic field up to 3000 Oe, which was realized using neodymium based permanent magnets [79]; this corresponds to the neat efficiency for the Gd-based TMG to be 1.46% due to its smaller Q_{in} and larger ΔM [80] in Eq. (1). It should be noted that TMG performance is dependent on temperature difference of the hot and cold reservoirs and for the optimal difference of 10 K the efficiency can further approach 2% for TMG based on $Gd_5(SiGe)_4$ compounds [81] (Fig. 5).

Recently, TMGs based on Heusler alloy films have been successfully developed with an increasing electrical power per footprint by a factor of 3.4; i.e., the electrical power per footprint reached 50 $\mu W/cm^2$ at a temperature change of only 3 K [65]. TMG performance can be increased via resonant actuation of freely movable thin-film devices based on the Heusler alloy Ni–Mn–Ga, which showed unprecedented power density of 118 mW/cm^3 with a periodic temperature change of only 3 K required for operation and the duration of thermomagnetic duty cycle of about 12 ms; this efficiency compares favorably with that of the best thermoelectric generators [82]. Gueltig et al. reported the TMG gadolinium prototype which exhibited an oscillation frequency of 0.33 Hz, a work output of 0.6 J/kg per cycle, and a power density of 0.2 W/kg under the temperature difference of 60 K [82].

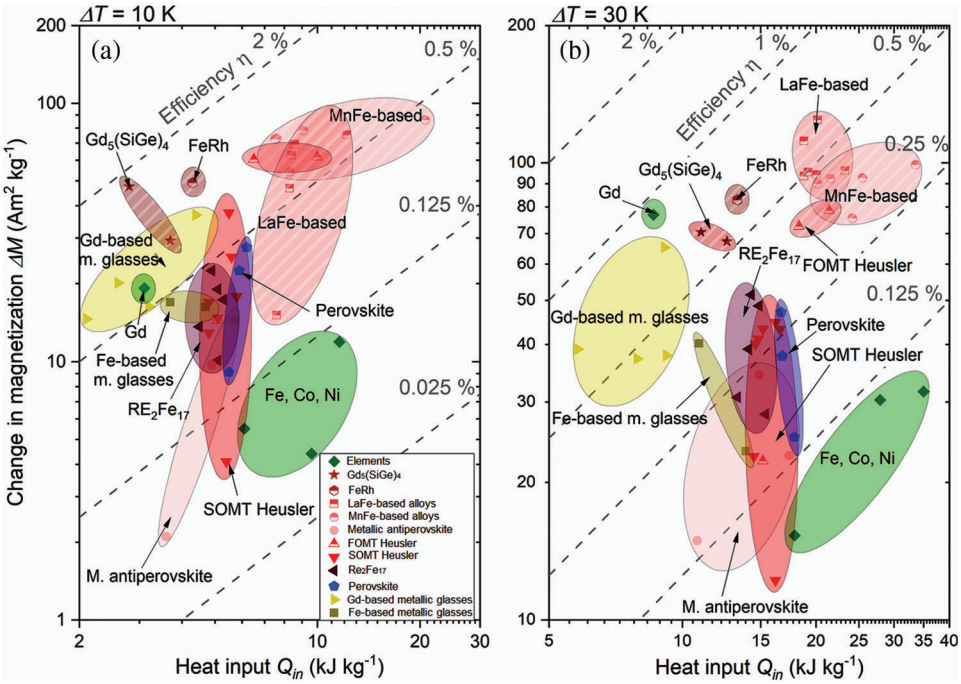

Figure 5: Thermodynamic efficiencies η of different thermomagnetic materials. To reach high η, a large change in magnetization ΔM is beneficial, as well as a low heat input Q_{in}. The gray dashed lines represent a constant efficiency $\eta = \mu_0 \Delta MH/Q_{in}$. Accordingly, the most efficient materials are located in the top left corner, where η approaches 2%. Material properties were evaluated for two different temperature spans in Ashby-type plots: (a) at $\Delta T = 10$ K, materials exhibiting a first order transition (half solid symbols) reach the highest efficiencies; (b) at $\Delta T = 30$ K, materials with a second order transition (solid symbols) become competitive. Metallic materials are displayed in shades of red, ceramics in blue, metallic glasses in shades of yellow, and elements in green. Reprinted with permission from [83] under Creative Commons Attribution (CC BY) license. Copyright 2021, Author(s)

3.4 Hydride Heat Engines

The hydride heat engine is based on the property of some metals and metal alloys, such as $LaNi_5$, $La_{0.8}Ce_{0.2}Ni_5$, Mg_2Ni, $TiMn_2$, TiFe, Pd, etc., to store hydrogen within their crystalline lattice through formation of a metal hydride. Hydration and dehydration processes are described by the reaction:

$$M + \frac{y}{2} H_2 \leftrightarrow MH_y + Q \tag{2}$$

where M is the metal used, MH the metal hydride, and Q the quantity of the reaction heat. The reaction (2) includes the following steps [84]: (i) physisorption of hydrogen molecules on the metal surface; (ii) dissociation of hydrogen molecules; (iii) penetration of hydrogen atoms from the surface into the crystal lattice; (iv) hydride formation by nucleation and growth; (v) diffusion of hydrogen atoms through the hydride layer, involving interstitial and/or vacancy mechanism.

The amount of hydrogen accumulated by metal hydride lattices is dependent on the temperature of the metal hydride; low temperatures facilitate hydrogen storing while high temperatures promote its desorption from the metal hydride. Their different storage capacity at different temperatures can be used to generate a hydrogen flow between two metal hydride storage media, i.e., a high-temperature metal hydride (HTMH) and a low-temperature metal hydride (LTMH), that are attached to each other through a hollow, sealed tube filled with hydrogen, where one medium desorbs hydrogen, while the other absorbs it (Fig. 6). The flow of hydrogen then can be converted into mechanical work of a pneumatic motor inserted into the closed-tube system; this work then can be converted to electrical energy through an electromagnetic generator. In this construction, each storage medium must be alternately heated and cooled to allow the hydrogen to circulate between the two media and to produce a cyclic motion of the generator, respectively, which is a particular disadvantage of this type of the heat engines [35].

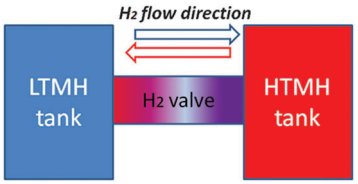

Figure 6: Scheme of the hydride heat engine in the form of the coupled HTMH and LTMH tanks by a hydrogen connection

Metal hydrides can offer several advantages over other thermochemical hydrogen storing materials (salt hydrates, metal hydroxides, oxides, and carbonates) due to the higher energy storage capacity and power density. The relatively high efficiency and reasonably low temperature difference between HTMH and LTMH yield the advantages of the metal hydride heat engines (Table 1). However, performance of metal hydride heat engines varies and is generally limited by reactor configuration, design, optimization and selection of appropriate thermochemical materials. Ham and coauthors improved thermal energy conversion via synchronous motion of the thermal waves and the heat source (or sink) inside paired porous media channels, which accompanied the phase transition in the succession of unit metal-hydride heat pumps [84]. For the best hydride pair of $LaNi_4Al$ and $TiV_{0.62}Mn_{1.5}$ coefficient of performance was calculated to be near 60%. Lototskyy et al. proposed combination of latent heat and thermochemical heat storage system based on two-tank metal hydrides [85]. The systems consisted of two metal hydride tanks coupled and equipped with a phase change material (PCM) jacket. The heat charging process activated desorption of hydrogen from HTMH, followed by its storing in LTMH. At the same time, the heat that

originates from the hydrogen absorption in the LTMH tank was stored as latent heat in a PCM jacket surrounding the LTMH tank, which can be reused during the heat discharging.

4 Thermoelastic Engines (Artificial Muscles)

Thermoelastic engines operate owing to specific molecular mechanisms in elastic materials such as polymers, leading to change in the polymer volume, i.e., its contraction or expansion, in response to electromagnetic irradiation of the material. The mechanisms of this change include molecular isomerization, conformational changes, cross-linking or disruption of intermolecular bonding, packing rearrangement, changes in chain segments mobility as well. The above processes can occur under irradiation of the material by different wavelengths; however, one should distinguish the processes induced either by light quanta of high energy, i.e., in the UV or visible region, or due to absorption of IR photons, i.e., heat [2]. In the first case, there is a relatively high barrier that corresponds to the energy gap of the π–π* or n–π* transition, where electronic excitation triggers molecular isomerization or cross-linking (Fig. 7). These processes are referred to as reversible photochromic or photochemical ones [86,87], where photoisomerization involves one-bond-flip or hula-twist mechanism, although no chemical bonds are broken, but the molecule only changes its shape, while cross-linking does break chemical bonds. The devices based on such processes will be referred to as photonic devices.

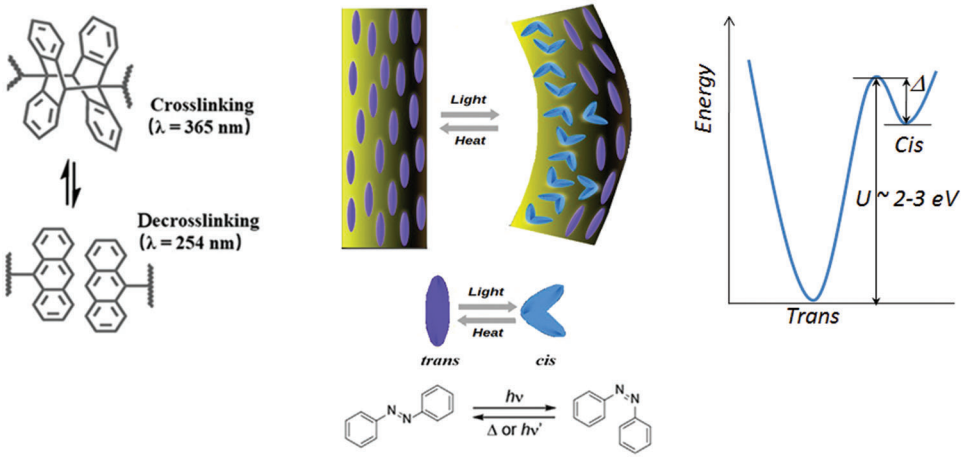

Figure 7: Illustration of photochemical mechanisms leading to elastomer deformation due to (a) crosslinking/decrosslinking and (b) isomerization mechanisms. (c) Potential energy profile of a photosensitive isomer showing relative potential barriers for the *cis* and *trans* configurations

In the second case, the energy is dispersed over molecular vibrations, and isomerization or other molecular processes are vibronic-induced; this will be referred to as thermal devices. The typical molecules employed in the above two processes are shown in Scheme 1.

Although the above photonic devices cannot be literally referred to as thermomechanical engines, their operational principle due to conversion of electromagnetic radiation to mechanical energy is very similar to the thermal devices (Fig. 7b); therefore, we consider them first.

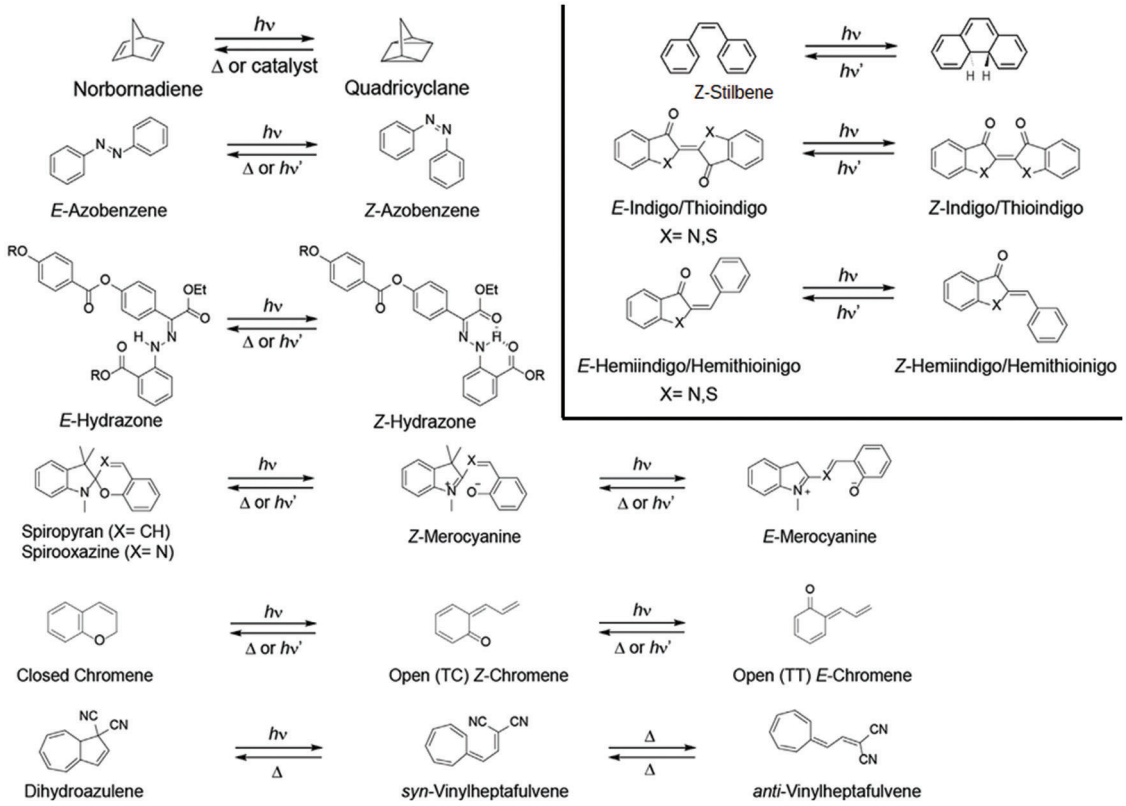

Scheme 1: Examples of isomerization processes for different molecules. The right upper corner indicates processes induced by UV-Vis light only, whereas for the others both light and heat can trigger isomerization

4.1 Actuation via Light-Driven Photochemical Mechanisms

Photonic devices based on light-responsive materials have been of great interest as they can be used in different applications such as optical memory [88–90], energy harvesting [91], light-driven robotics [92,93], micro-electromechanical systems and actuators [94]. The majority of photonic devices operate due to photochemical switch between *cis* and *trans* isomers of specific molecules [95] (see Scheme 1). Such molecules often constitute of azobenzene moieties which possess good thermal stability, well separated absorbance bands of the *trans* and *cis* isomers, a relatively rapid reversible thermal *cis–trans* conversion as well. In this moiety, bearing two phenylamines, whose nitrogen atoms are linked together by a double bond forming an axle, the optical excitation induces a clockwise rotation of a photoisomerizable group around the molecular axle, triggering a thermally stable elongated *trans* configuration towards a meta-stable bent *cis* form [96]. The thermal activation step then converts the unstable *cis* isomer back to the stable *trans*-isomer form.

Fine details of azobenzene photoisomerization have been disclosed recently. This process was described as an "inversion-assisted torsion" along a torsional coordinate around the central C−N = N−C moiety, which is assisted by C−N=N bending modes [97]. During the isomerization, the phenyl rings remain roughly stationary, while the central C−N=N−C moiety rotates and moves between them in a pedal-type motion, while the phenyl rings also follow this motion, but on a much slower timescale compared to the central moiety. As a result, the rings remain still out of plane when the central CNNC dihedral angle has reached 180°, but they continue to twist after the main isomerization event has finished [98].

Besides *cis*/*trans* isomerization mechanism, photo-crosslinking (photodimerization) and decrosslinking (photocleavage) can be responsible for the photoinduced actuation in some materials as well (Fig. 7). Jiang et al. demonstrated this process on the example of an anthracene-containing liquid crystal polymer, where the anthracene pendant groups were responsible for reversible photodimerization and dimer photocleavage under exposure at two different wavelengths in the UV range, which yielded reversible deformation of the polymer, respectively [99].

Recently, a number of small photochromic molecular switches responsible for a photoinduced motion have been demonstrated (see Scheme 1) [100–108]. Besides, more complex photochromic moieties have been proposed as well. For example, Kajiya et al. designed photoresponsive inorganic–organic hybrid molecules consisting of diarylethene and polyhedral oligomeric silsesquioxane linked by amide bonds, which showed an enhanced conversion ratio from the open- to the closed-ring isomers upon UV irradiation in a solution [109]. Synthesis of photoactive block copolymer containing 1-(2-hydroxyethyl) −3,3-dimethylindoline- 6-nitrobenzopyran (SP) as a photochromic agent and ZnS nanoparticles (NPs) as a mediator for photo-optical switch of the SP derivative to the open form due to the interaction with the NP surface was reported by Pizarro et al. [110].

The nanoscopic structural movement of isomerizing molecules can be translated to macroscopic motions of organic crystals and amorphous materials that comprise the photochromic compounds [111–117]. For example, Morimoto et al. demonstrated macroscopic mechanical work through the photoinduced movement of a light-driven actuator in the form of a millimeter-sized two-component cocrystal composed of diarylethene derivatives [118]. However, to perform macroscopic mechanical work, for example, in the form of mimicking human muscle-like motion by artificial actuators, the material should be soft and deformable in response to external stimuli, such as temperature and light. Polymer, liquid crystal elastomer (LCE) and liquid crystal network (LCN) materials satisfy this requirement and can serve as a matrix for photo-switchable molecules [119]. LCEs and LCNs have additional advantage due to their inherent anisotropy which amplifies the mechanical properties and can serve as a trigger for reversible mechanical deformations through order parameter reduction or reorientation of the network [120]. LCEs exhibit good thermoelastic properties. Particularly, when heated above the nematic–isotropic phase transition, LCEs contract along the alignment direction of their mesogens, but expand by cooling below the phase transition temperature (Fig. 8). By combining the thermoelastic properties of LCEs with photoinduced changes in the molecular volume of incorporated photochromic molecules such as spyropyranes, azobenzenes, stilbenes, fulgides, diarylethylenes, the light-induced deformation of the LCE composite material is highly feasible [121]. Finkelmann et al. demonstrated that an azobenzene containing LCE that has a polysiloxane main chain, experiences contraction as much as 20% upon exposure to UV light due to the *trans–cis* isomerization of the azobenzene moiety [122].

The introduction of photochromic molecules into LCNs yields novel composite materials (such as azo-LCN) that have found various applications where light input is converted into mechanical output [123–127]. Application of azo-LCN as a photodriven polymer oscillator with a frequency as high as a hummingbird wing beat (20–80 Hz) was reported by White et al., where the demonstrated polymer cantilever consisted of a monodomain azobenzene containing LCN [128]. The oscillation of the azo-LCN cantilever could be turned on and off by switching the polarization direction of the driving laser beam, and it has been considered to be prospective for application in light energy harvesting devices [129]. Yue et al. [130] exploited a “photomelting” azobenzene monomer cross-linked into the LCNs to fabricate photoresponsive polymer films that were able for photomechanical actuations and demonstrated reversible photoswitchable glass transition temperatures (T_g) in response to the UV/visible light exposure. The T_g of the polymer network was higher than room temperature in the *trans*-form and lower than room temperature in the *cis*-form; thus, the bending mechanism operated via the photoswitchable T_g. Gelebart et al. by achieving fast *cis*-to-*trans* thermal relaxation of modified azobenzene moiety incorporated into azo-LCNs demonstrated

generation of continuous, directional, and macroscopic mechanical waves under constant light illumination, with a feedback loop that was driven by self-shadowing; this was proposed for potential application in light-driven locomotion and surfaces self-cleaning [131]. Other applications of azo-materials include their exploiting as photomechanical light harvesters that operate at relatively high frequencies [132], soft robotic relays of LCE/PEDOT:PSS photomechanical conductive bilayers [133], mesoscale photomechanical optical fibers [134], transduction of photomechanical deformation into piezoelectric signal for the generation of electrical energy [135], photomechanical pendulum that produces electric current in a coil wrapped around its end when allowed to oscillate in a static magnetic field [136], surface engineering and lithography (light-induced directional mass migration) [95], capture of CO_2 by light-responsive ionic liquids through reversible *trans–cis* isomerization [137], etc.

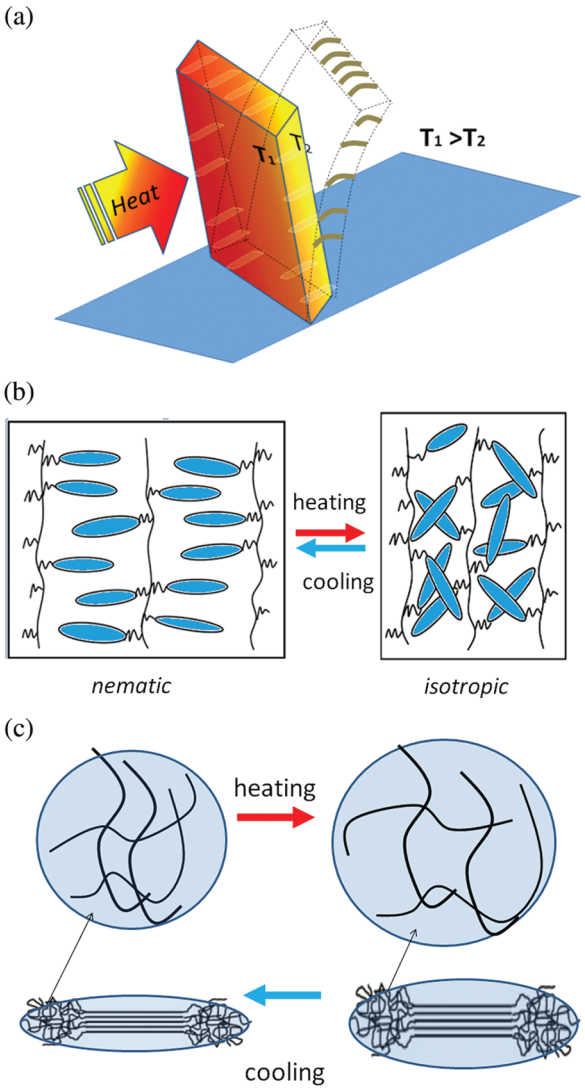

Figure 8: (a) Illustration of mechanical changes upon inhomogeneous heating of an elastomer strip with molecular mechanisms indicated for (b) liquid crystal elastomers with negative thermal expansion (redrawn from [138]) and (c) polymers with positive thermal expansion. In (c), both crystalline and amorphous regions are indicated

4.2 Actuation via Thermally Induced Isomerization

There are different examples of materials, where a low-grade heat can induce molecular isomerization via specific processes such as thermally-induced isomerization in non-conjugated linoleic and α-linolenic acids [139,140], trilinolein and trilinoelaidin at 250°C [141], carbon disulfide dimer anions [142], (*E/Z*)-isomerization of *retro*-carotenoid rhodoxanthin [143], water-assisted *linear*-to-*cyclic* isomerization of donor-acceptor Stenhouse adducts [144], thermally-induced isomerization between all *E*- and *Z*-isomer-rich xanthophylls [145], and even isomerization of CdS magic-size clusters which have identical cluster masses but slightly different structures, whose interconversions follow first-order unimolecular reaction kinetics [146]. In most cases, *trans*-isomer is considered to be stable; however, stable *cis*- coordination complexes, such as (*cis*-L)$ZnCl_2$ and (*cis*-L2)$M^{II}Cl_2$ [M = Fe, Co, Ni] have been recently reported also, which are converted to their *trans*-1,2-bis(1-R-benzo[*d*]imidazol-2-yl)ethene (R = H or R = CH_3) ligands using high-energy UV light, whereas the *trans*-to-*cis* isomerization is induced thermally [147].

Thermally induced *cis*-to-*trans* isomerization kinetics for azo-compounds is usually slow, having the time constants from minutes to days; however, this kinetics can be greatly accelerated by attaching specific substituents to the azo-dyes structures [148]. By minimal modifications of the arylazoindole core via methylation, Simeth et al. were able to dramatically change the *Z*-to-*E* thermal isomerization rate from days to a nanosecond time scale [149]. They also showed fine-tuning of the *Z*-to-*E* lifetimes through choosing a proper dimethyl sulfoxide–water (or buffered water) solvent mixture. Azo dyes that possess a strong push–pull configuration and provide an azo–hydrazone tautomeric equilibrium were shown as promising chromophores that demonstrate fast thermal *cis*-to-*trans* isomerization kinetics at room temperature. Garcia-Amoros et al. reported a synthesis of a new highly biocompatible pyrimidine-based azophenol that exhibited nanosecond thermal-relaxation times of *cis*-to-*trans* isomerization at 298 K, i.e., at temperatures close to physiological conditions, which gives a clear perspective for its biological and medical applications [150]. Poutanen et al. [151] showed acceleration of the thermal *cis–trans* isomerization rate through hydrogen bonding of the azobenzenes, which makes this effect applicable for high sensitive humidity sensor with quick response to relative humidity changes. It was reported that thermal decay of the metastable *cis* isomers of the other photochromes, mono-arylated indigo derivatives, can be greatly accelerated by a factor of 300 by using a small amount of water [152]. Another elegant approach to accelerate *cis*-to-*trans* isomerization rate is coupling of molecular switches and metal nanoparticles. Titov et al. found that the interaction of the azobenzene-containing molecules with gold nanoparticles leads to decreasing thermal lifetimes of the *cis* isomer by up to 3 orders of magnitude in comparison to the lifetime of the free molecules separated from Au nanoparticles [153]. This effect was explained by lowering activation barriers for azobenzene-containing molecules due to either electron injection or withdrawal, which promotes a dramatic increase in the thermal isomerization rate.

Depending on the photochrome used, the back-conversion *cis-trans* reaction can release heat energy via triggering by different processes, including catalytic and electrocatalytic ones [154,155]. A high-energy metastable state in photo-isomers can be considered as energy storage, where up to 21% of the solar energy can be stored as chemical energy for the later heat production [156]. Recently, Wang et al. demonstrated a combination of solution- and neat-film azobenzene-based molecular solar thermal systems, where solar energy can be stored as chemical energy for as long as one month and released as heat, with a solar energy storage efficiency of 0.5% and with power output up to 0.1 nW (with a power output per unit volume up to 1.3 W/m^3) [157].

4.3 Thermally Induced Actuation with Positive Thermal Expansion

Thermally induced reversible process of the material expansion due to the changes in molecular mobility leading to repulsion between molecules and packing rearrangement upon heating can be used for harvesting and storing IR energy in the form of mechanical energy of deformation. In order to realize this idea the heat

absorber must be a deformable material that possesses a high thermal expansion coefficient. Best materials for this purpose are polymers and elastomers, whose thermal expansion coefficients are one order of magnitude larger and their thermal conductivity is 2–3 orders of magnitude lower than that of metals (Table 2). The only exception can be found for some metal alloys whose thermal expansion coefficients are comparable with that of polymers [158] (Table 2). Owing to the low thermal conductivity, polymer material can be heated inhomogeneously, when one side of the material is exposed to heat, while the other side remains relatively cold. Thus, a free polymer strip, when exposed to heat/IR energy from one side, tends to bend due to the poor equalizing of temperature across the sample and therefore different expansion of the material at the opposite sides of the strip (Fig. 8a). The dominant physical mechanism of this thermomechanical effect is due to producing a temperature gradient across the strip thickness that causes strip bending as a result of uneven thermal expansion distribution across the strip. Layers closest to the front side of the strip expand more than layers of the rear side, causing bending. Thus, polymer materials can transduce thermal energy into mechanical stress by the macroscopic deformation of the sample, i.e., thermomechanical effect. Many polymers and elastomers with positive thermal expansion coefficients possess additional advantageous properties, such as high processability, flexibility, easy fabrication characteristics, large deformation and power density, low manufacturing costs, which are required for fabrication of artificial muscles [159–162].

Nylon-made coiled actuators representing specific type twisted polymeric fibers were reported to have excellent thermo-mechanical characteristics, such as hysteresis, repeatability, predictability, high stored elastic energy, large deformations when heated, together with promising performance in terms of energy and power densities [163]. Particularly, the maximum elastic energy density up to 2.1 kJ/kg, can be stored in nylon coils, which is much higher than that in steel springs (up to 0.9 kJ/kg). Haines et al. discovered a new class of thermo-mechanical actuators based on drawn polymeric fibers (mostly nylon), commonly employed as fishing lines and sewing threads [164]. Specifically, Haines and coauthors demonstrated the relationship between temperature-induced deformations and twisted/coiled configuration of these fibers, which showed outstanding performances with energy densities as high as 2.63 kJ/kg and power densities over 5.3 kW/kg (Table 1), and strokes up to 50%, which can be employed both in linear and rotational actuators. Chou and coauthors showed that the coiled polyethylene-terephthalate (PET) artificial muscles exhibit stress softening and their nominal activation energies represent linearly decreasing functions of the training load [165].

Many actuators, however, are based on multifunctional materials, where mechanical actuation in response to the thermal energy input is provided by synergetic action of two components. Combination of nickel-titanium alloys and polymers represents the well-known hybrid thermo-mechanical SMA actuators which recover their deformation when heated above a certain temperature [166]. Such a shape-memory effect combines a thermoelastic martensite-austenite phase transition in the Ni-Ti alloy and a variation of conformational entropy in the shape memory polymer [47].

On the other hand, different fillers that assist effective heating of the polymer matrix were also actively used. For example, absorbers such as carbon nanotubes (CNTs), silver, gold and magnetic Fe_3O_4 nanoparticles, etc., were exploited as nano-heaters [167–169]. Specific action of magnetic NPs dispersed in the polymer matrix facilitates nanocomposite heating, thus triggering its shape recovery, when being undergone by an applied oscillating magnetic field or radio frequency (RF)-microwave radiation. In contrast to CNTs and other strongly adsorbing species, the temperature dependence of magnetic susceptibility of magnetic NPs effectively creates a self-limiting processing that fundamentally restricts the maximum temperature above which magnetization ceases [170]. Carbon fibers added to the silicone matrix in an ordered manner serve as specific filler which renders a dual effect of promoting heating as well as controlling polymer deformation; the latter is strongly dependent on the fiber orientation in the sample [73]. Jia et al. observed that a photo-thermal effect of CNTs incorporated to the polyurethane

matrix is accompanied by a self-healing effect in this flexible matrix, which can find corresponding application in electronics [171], because the self-healing of the above nanocomposite could be induced precisely, remotely and efficiently under irradiation by NIR laser without influencing the undamaged areas. The healing efficiency of the composite containing 3 wt% CNTs was shown to reach 90.1% [171]. In addition, the conductive layer coated onto the nanocomposite surface could also be recovered under irradiation. Dai et al. fabricated a self-healable hybrid yarn based on the silicone elastomer as a guest material, where improved material's environmental adaptability and a work capacity of 0.49 J/g, which is 12.7 times that of the natural muscle, were demonstrated [172].

Table 2: Thermal expansion coefficients and corresponding thermal conductivity of selected materials. Description of materials with the largest thermal expansion coefficients is given in the text

Material	Coefficient of thermal expansion, 10^{-6} m/m K	Thermal conductivity (W/m K)
Poly(N-isopropylacrylamide) (PNIPAM) hydrogel	~25000	0.35–0.51 [173]
Shape-persistent polyphenylene equipped with peripheral dodecyl chains	980	
Porous coordination polymer (see text)	482	
Paraffin wax	106–480	0.15–0.3
Silicone rubber	250–300	0.14–0.63
Ethylene ethyl acrylate copolymer (EEA)	205	0.42
Gutta percha	198	0.4–0.9
Ethylvinylacetate (EVA)	180	0.08
Polyvinylidene fluoride (PVDF), 50%–60% crystalline	128–140	0.1–0.25
Polyethylene (PE)	108–200	0.33–0.52
Ti–36Nb alloy	163.9*	
Fluorinated ethylene propylene (FEP)	135	0.21
Cellulose acetate (CA)	130	0.16–0.36
Polyethylene terephthalate (PET)	124	0.15–0.4
Polytetrafluorethylene (PTFE)	112–135	0.25
Polyamide (PA, isotropic)	110	0.24–0.3
Celluloid	100	0.12–0.21
Aluminium	25	237
Graphene	−8	~4000
Graphene oxide	−67	72–670 (depending on the oxidation degree)
Ti–36Nb alloy	−95*	
$Sm_{2.75}C_{60}$	−100	
$Ni_{54}Mn_{25}Ga_{21}$	−105*	

(Continued)

Table 2 (continued)

Material	Coefficient of thermal expansion, 10^{-6} m/m K	Thermal conductivity (W/m K)
$Ag_3Co(CN)_6$	−130*	
(S,S)-octa-3,5-diyn-2,7-diol	−204*	
Polyamide (PA610, fiber)	−400*	0.24–0.3
s-dibenzocyclooctadiene (DBCOD)	−1200	

Note: *anisotropic material; thermal expansion coefficient is shown along a specific axis.

4.4 Thermally Induced Actuation with Negative Thermal Expansion

There are several processes that induce negative thermal expansion (NTE) of materials. First, these include transverse vibrations of atoms in complex structures such as zeolites, metal organic frameworks (MOFs), porous coordination polymers, etc. Here, a central linking atom in the chain $M1\cdots O(F)\cdots M2$ vibrates perpendicular to this chain upon heating, which results in the shrinkage of the distance between $M1\cdots M2$, thus yielding the NTE behavior of the material [174]. A similar NTE mechanism was also found in 2D materials such as graphene, where NTE is dominantly caused by the significant transverse vibration effect owing to large out-of-plane fluctuations [175,176].

The second factor leading to NTE is geometric flexibility of the material structure. For example, LCE materials possess crystalline ordered network and structural transformability, which is bistable or multistable; therefore, heating can induce change from the ordered structure, for example, nematic structure with distance-tolerant position of mesogenic units, to isotropic disorder, where these units do not obey the above distance and where the material displays dynamic framework deformation [138]. Here, the existence of large pores in the LCE structure provides extra space for the thermal motion caused by geometry deformation (Fig. 8b).

Third, host-quest materials are able to display the NTE behavior as well. These materials are complex systems constructed by two or more molecules or ions that are held together through noncovalent interactions, where the existence of guest molecules in the pores may largely influence the thermal expansion behavior. The examples include $ZnPt(CN)_6$ with guest water molecules, $Cd(CN)_2$ with different occupancies of CCl_4 guests, intercalation of Li^+ into $Sc_{0.9}Fe_{0.1}F_3$, etc. [174]. In these materials, heating results in desorption of the guest molecules, which yields shrinkage of the lattice framework, respectively.

Spin crossover (SCO), also known as spin transition, is the fourth factor able to induce the NTE. This phenomenon usually takes place in materials containing $3d^4$~$3d^7$ transition metal complexes, where the spin state can switch between low spin and high spin under external stimuli including temperature [177]. The variation of 3d electron configurations leads to the changes of bond length and unusual volume changes in SCO systems, respectively. Examples of SCO materials include $Fe[Au(CN)_2]_2$, which possesses hinge like motif with iron(II) as the screw, where the spin state changes of Fe(II) largely influence the conformation of the framework [178].

NTE that occurs via molecular rearrangement is caused owing to weak intermolecular interactions in molecular systems, coupled by van der Waals forces, π…π interactions, halogen-halogen interactions, as well as hydrogen bonds [179,180]. These weak bonds compared to the covalent bonds, are sensitive to temperature changes, leading to large structural rearrangements. A relevant example can be taken from the ice structure, where disruption of weak hydrogen bonds upon heating results in liberation of water molecules which then occupy inter-site space, thus leading to contraction of the volume. A similar behavior was found in the dumbbell shaped molecules of (S, S)-octa-3,5-diyn-2,7-diol stacked in columns

along *c*-axis and connected through hydrogen bonds in their 3D network structures (Table 2). This structure has a considerable sheath of empty space around each molecule, so that heating leads to a rare biaxial NTE behavior [181]. Unusual anisotropy in thermal expansion behavior was observed in liquid crystal cobalt octakis(ndecylthio) porphyrazine thin films (CoS_{10}) which exhibited 2D NTE in the transverse plane, but positive thermal expansion along the column axis [182]. This was explained by the tilting of the porphyrazine cores and contraction of side chains which together provide the 2D NTE, whereas the increasing cofacial distance and tilting of core yields the 1D positive thermal expansion along the column. Similar thermal expansion anisotropy was observed in nylon fibers, which demonstrated the negative expansion along the fiber axes but positive radial expansion [183].

Conformational change is another mechanism leading to NTE behavior. The most known thermo-responsive polymer with NTE is poly(N-isopropylacrylamide) (PNIPAM). This polymer is hydrophilic below 32°C, but it is hydrophobic when the temperature is higher than 32°C. The hydrophilic chains exist as single chains with expanded coil conformation, while the hydrophobic PNIPAM chains transform into single chain globules or multichain aggregates accompanied with a large thermal contraction [184]. Recently, specific conformational changes of dibenzocyclooctadiene (DBCOD) derivatives, responsible for the NTE properties, were found. In DBCOD, the conformations occur between chair (C) and twist-boat (TB) forms, leading to thermal contraction of DBCOD when the TB conformation is able to turn into C conformation with temperature increase, and when the volume of C conformation is smaller than the volume of TB conformation [185].

It was claimed that introducing molecular asymmetry can reduce crystallinity significantly and consequently facilitates the kinetics of the conformational change which leads to the large NTE. Shen et al. revealed a giant negative thermal expansion coefficient of ~ -1200 ppm K^{-1} at ambient or near ambient temperatures for a polyarylamide film containing DBCOD. This film revealed unconventional and completely reversible thermal contraction under low-energy stimulation, which exceeded that for any known negative-thermal-expansion materials under similar operating conditions [186]. The origin of the above abnormal thermal shrinkage was assigned due to the conformational change of the DBCOD moiety, which occurs from the thermodynamic global energy minimum in the TB to a local minimum in the C conformation. Even a larger NTE was measured for the DBCOD-based polymer systems, which was in the range from -1140 to -2350 ppm K^{-1} [187]. This effect was claimed to open a new pathway for creating NIR-based macromolecular switches and motors, as well as devices for ambient thermal energy conversion and storage.

5 Emergent Thermomechanical Devices

5.1 Shape-Programmable Actuators

The concept of shape programming exploits the difference in thermal expansion coefficients of different components in a multicomponent actuator possessing multiple degrees of freedom and thus provides its programmable shape control according to its differential design architecture upon exposure to light or heat. Gao et al. exploited the humidity-dependent nonlinear coefficient of thermal expansion of GO in fabricated graphene oxide/ethylene cellulose (GO/EC) bilayers that indicated a rapid temperature-dependent photothermal actuation and a programmable 3D origami shape control (Fig. 9a). In the above bilayer structure, GO served as a NIR-active layer with negative thermal expansion coefficient, whereas EC as a layer with positive thermal expansion when exposed to heat. The developed strategy allowed the authors to construct complex systems with the remote control of their 3D shapes, such as a rapid blooming rate in bionic flowers, which in fact represented mechanical metamaterials with auxetic behavior [188].

Motion that depends on the direction of the triggering stimulus and that autonomously and self-sufficiently reacts to changing environmental stimuli in a direction-dependent manner is the core of smart biomimetric actuators [189]. Artificial heliotropic devices with no additional mechatronic components and resultant energy consumption, which are able to follow sunlight and which can be used for increased light

interception, have been demonstrated by Li et al. [190]. The heliotropic devices were constructed from a novel reversible photo-thermomechanical LCE–single-wall carbon nanotube (SWCNT) nanocomposite that was able to be directly driven by natural sunlight and that possessed strong actuation capability. When such an actuator faced the sun, it contracted, leading to tilting an attached solar cell towards the sun, thus demonstrating an artificial heliotropism. Using the LCE nanocomposite actuators, the artificial heliotropic devices showed full-range heliotropism in both laboratory and in-field tests. As a result, significant improvement in the photocurrent output from the solar cells attached to the artificial heliotropic devices was observed.

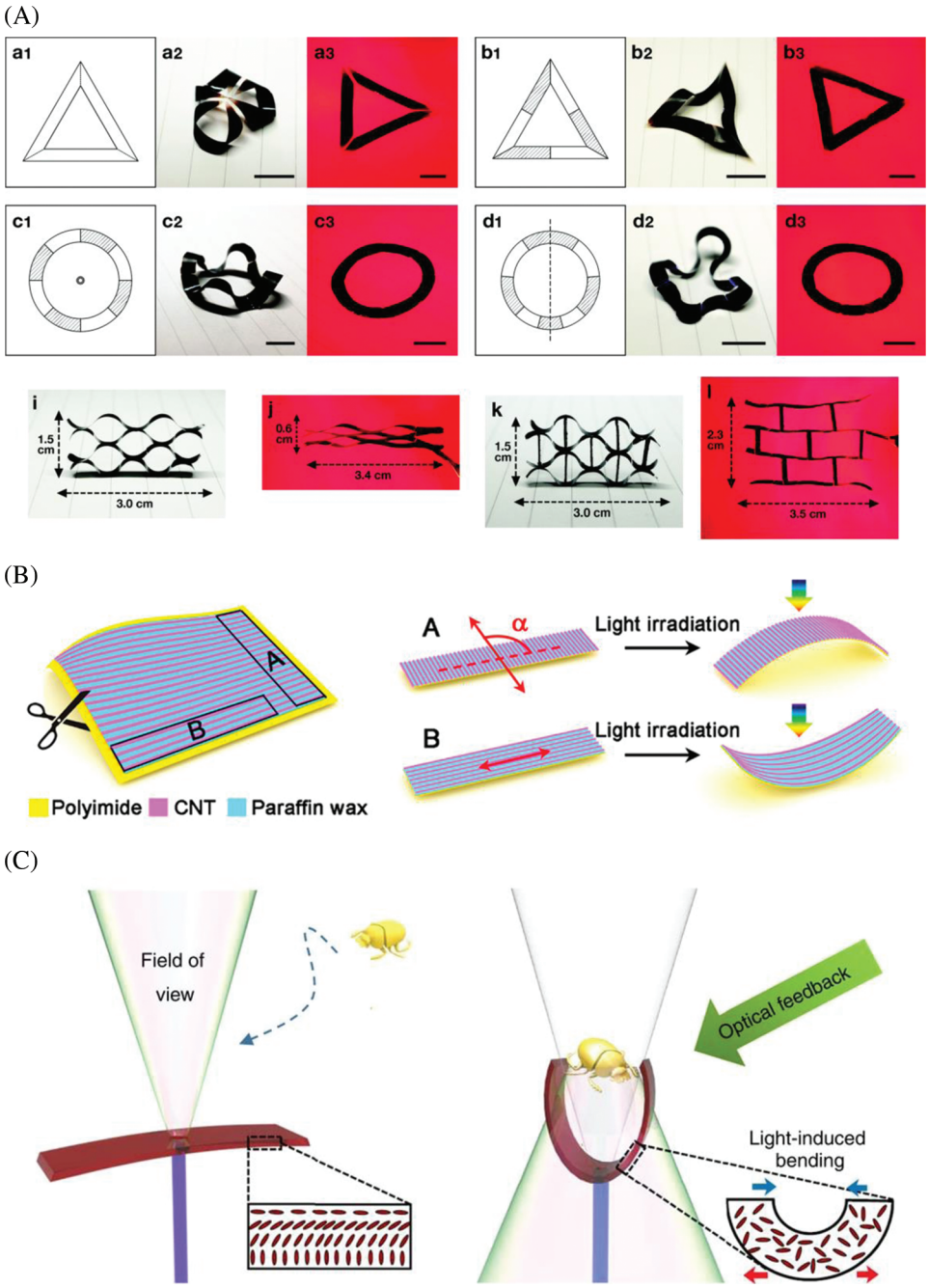

Figure 9: (A) Various shape programmable 3D architectures derived from 2D layouts. (a–d) Graphic designs, room temperature stable 3D modes and high temperature planar states of (a) an equilateral

Figure 9 (continued)
triangular ring encoded with only positive curvature; (b) an equilateral triangular ring encoded with alternating positive and negative curvatures; (c) an annulus programmed with central symmetry; and (d) an annulus programmed with axial symmetry; scale bars is 1 cm. (i–l) 3D-PTA enabled mechanical metamaterials including (i and j) an assembly strategy for ultra-positive Poisson's ratio and (k and l) an assembly strategy for negative Poisson's ratio. The length direction of the stripe is regarded as the axial direction for Poisson's ratio calculation. All demonstrations shown above were fabricated with 10 μm GO and 30 μm EC. Reversible actuations were performed under the 200 mW cm^{-2} NIR irradiation. Reprinted with permission from [188]. Copyright 2020, Royal Society of Chemistry. (B) Schematic illustration of the apheliotropic and phototropic bending of the composite strips with different aligned directions of carbon nanotubes. Reprinted with permission from [191]. Copyright 2016, American Chemical Society. (C) Left: Schematic drawing of the light-triggered artificial flytrap at its open stage, when no object has entered its field of view. No light is back-reflected to the LCE actuator, which remains in the open stage. Right: The flytrap closes when an object enters its field of view and causes optical feedback to the LCE actuator. Light-induced bending of the LCE leads to closure action, thus capturing the object. The insets show the schematic molecular orientation in LCE actuator at the open and closed stages. Reprinted with permission from [192] under the Creative Commons Attribution (CC BY) license (http://creativecommons.org/licenses/by/4.0/). Copyright 2017 by the Author(s)

Deng et al. presented a general strategy effective for fabricating visible-light-responsive actuators with diverse and tunable deformations by embedding aligned CNTs in the paraffin wax on a polyimide substrate [191]. The synergy of the above two components made it possible mimicking plant operation, where aligned CNTs functioned as cellulose fibrils, and the paraffin wax resembled the soft cells/tissues of a plant. It was demonstrated that various motions of photomechanical actuations, i.e., phototropic/apheliotropic bending to three-dimensional helical buckling can be controlled by tuning the CNT alignment direction (Fig. 9b). An additional benefit of using the CNTs was their ability to absorb infrared and visible light, endowing the resultant actuators with rapid responsiveness. The reported photomechanical actuators also demonstrated controlling a mechanical arm and functioning in an energy harvesting system to execute complex but well-controlled motions.

An autonomous soft self-regulated actuator that is able to mimic the action of a flytrap plant when exposed to light and that uses optical feedback to trigger photomechanical actuation was demonstrated by Wani et al. [192]. The flytrap was designed using a light-responsive LCE, fabricated onto the tip of an optical fiber, which acted as a power source and served as a contactless probe that senses the environment. Mimicking natural flytraps, this artificial flytrap was capable of autonomous closure and object recognition (Fig. 9c). It enabled self-regulated actuation within the fiber-sized architecture, thus opening up avenues towards soft, autonomous, and small-scale devices.

5.2 Breathing Frameworks

An alternative to thermoelastic thermal expansion is a large reversible volumetric change or material "breathing" that is thermally induced by solid-to-solid phase transitions (SSPTs). The SSPT process does not change the state of matter, but it usually occurs as a change in the material symmetry via relatively large internal shifts, leading to significant, up to several percents, volumetric changes, whereas thermoelastic expansion yields much smaller volumetric changes of the order of 10^{-2}% at best (see Table 1). For example, SSPT in silicate group materials, such as olivine Mg_2SiO_4, being abundant in the Earth's crust, under the pressure gives rise to the other denser polymorph, i.e., spinel. The solid transformation from olivine to spinel produces an appreciable change in volume (~8%), which is regarded as the cause of deep-focus earthquakes [193].

Recently, some metal-organic frameworks revealed large volumetric changes via SSPT. MOFs represent an exciting new class of nanoporous crystalline solids constituting metal ions/clusters combined with multifunctional organic linkages, which self-assemble at molecular level and generate a variety of ordered 3D structures. Bailey and Tezcan demonstrated protein–metal–organic frameworks (protein-MOFs) in the form of chemically designed protein crystals, composed of ferritin nodes predictably assembled into 3D lattices through coordination of various metal ions and ditopic, hydroxamate-based linkers [194]. The designed protein-MOFs possess extremely sparse lattice connectivity owing to their unique tripartite construction, leading to unusual thermomechanical properties, particularly, highly cooperative crystal-to-crystal transformation with a large volumetric change. Bailey et al. demonstrated reversible cycling of fdh-Ni-ferritin lattice expansion/contraction near-room temperature, with a 4% volumetric change within only 1°C and a hysteresis window of ∼10°C. This highly cooperative crystal-to-crystal transformation, which occurs due to the soft crystallinity of ferritin-MOFs, was proposed to provide the advantage of modular construction strategies that assist in discovering novel materials with tunable properties [194].

Maspoch et al. designed an open-framework $Cu_3(PTMTC)_2(py)_6(CH_3CH_2OH)_2(H_2O)$ structure, called MOROF-1, which combines very large pores with size of 2.8–3.1 nm and a bulk magnetic ordering [195]. MOROF-1 showed a reversible and highly selective solvent-induced 'shrinking–breathing' process accompanied by the large volumetric changes (25%–35%) and also the changes in magnetic properties.

Smets et al. reported thermally induced SSPT occurring in enantiotropically related polymorphs of molecular crystals composed of linear-chain amino acid racemates [196]. It was shown that shorter (quasi)racemates possessed larger (absolute) volume changes, which was assigned to the disorder change in the crystal structures. The maximum transition volume changes of ∼12 $Å^3$ per unit cell was found for (quasi)racemates with five carbon atoms per molecule. Different mechanisms of the SSPT were proposed, i.e., the torsional changes that occur in a molecule-by-molecule fashion and cooperative motion of multiple molecules at the same time without torsional changes. The latter is different from the classical first-order transition and occurs via motion of layers with respect to each other without changing the layer structure itself, which is enabled by the strong hydrogen bonding within the layers and the weak van der Waals interactions between them.

Recent strategies were also directed towards synthesis of hyper-expandable porous materials with remarkable framework flexibility and record thermal expansion coefficients [197]. Zhou et al. [198] synthesized guest-controlled multimode porous polymer framework based on dinuclear $Cd_2(RCOO)_4(L_{py})_4$ (L_{py} = pyridyl group) unit, which interconnected with eight neighbors through four $34pba^-$ and four $44pba^-$ ligands, resulting in a 3D coordination network with a uninodal 8-connected **bcu** topology. Due to the 3D hinge-like framework and quasi-discrete ultramicropores, this flexible porous coordination polymer exhibited both drastic guest-modulation effect and anisotropic expansion with record positive/negative thermal expansion coefficients of $+482/-218 \times 10^{-6}\ K^{-1}$ (Table 2). This enormous effect was assigned due to the jack-like motion of the guest supramolecular dimers, being analogous to the anisotropic thermal expansion of bulk van der Waals solids, which is crucial for changing the flexibility mode and thermal expansion behavior of the crystal.

Scherb et al. [199] reported exceptionally large thermal expansion in supramolecular polymer network assembled into an organized order, where the flexible organic architecture with high adjustability and weak intermolecular interaction exists in assemblies. This architecture represented a 2D supramolecular network on Au(111), consisting of shape-persistent polyphenylene molecules equipped with peripheral dodecyl chains, and this polymer system showed a giant thermal expansion coefficient of $980 \pm 110 \times 10^{-6}\ K^{-1}$ (Table 2).

Kim et al. [200] developed a PNIPAM hydrogel with a layered structure consisting of cofacially oriented electrolyte TiNS nanosheets. In the PNIPAM hydrogel, in the absence of substantial water uptake and

release, the distance between the nanosheets increases and decreases rapidly on heating and cooling, respectively, leading to significant expansion and contraction of the hydrogel; this represents a unidirectionally proceeding actuator that operates without the need for external physical biases. As a result, the hydrogel revealed unprecedentedly large, rapid, and anisotropic thermal expansion up to $\sim 25000 \times 10^{-6}\ K^{-1}$ due to the electrostatic repulsion between TiNS nanosheets (Table 2).

MOFs are ideally suited to host photoswitchable guest molecules, because the MOF inherent porous structures provide enough space where photoswitchable molecules can isomerize. Furthermore, due to the structural "breathing" of SSPT frameworks, the space within the pores undergoes significant changes, which can be exploited to facilitate or to trigger isomerization of guest molecules, where significant changes in molecular geometry are required. Griffiths et al. demonstrated a specific MOF with quest azobenzene (AB) photoswitches in the MOF pores with four different AB loading, specified as $1 \supset AB_{0.3}$, $1 \supset AB_{0.5}$, $1 \supset AB_{0.9}$, and $1 \supset AB_{1.0}$, respectively. This structure could work as a hybrid solar thermal fuel (STF) and solid−solid phase-change material (ss-PCM) [72]. Upon irradiation with 365 nm light, 40% of the AB guests converted from the *trans* to the higher-energy *cis* isomeric form in $1 \supset AB_{1.0}$, whereas the stored energy could be released upon heating the metastable *cis* isomers while balancing the endotherm associated with the phase transition. A net energy release over a full heating −cooling cycle was obtained with the maximum energy density of 28.9 J/g for the fully loaded $1 \supset AB_{1.0}$ composite, which is much better compared with energy density produced by traditional thermomechanical engines (see Table 1). The MOF composite with *cis*-AB guests showed also negligible thermal reconversion during 4 months at ambient temperature, which corresponded to an estimated energy storage half-life of 4.5 years, which is suitable for potential application of this composite MOF in STF. As a result of AB loading, the orthorhombic to tetragonal SSPT gave rise to volumetric changes of this "breathing" MOF up to ∼11%, with *cis* isomer of the guest molecules being stable when contracting the pores. In addition to the guest loading effect, the thermally induced reversible phase transition was observed for the $1 \supset AB_x$, systems, characterized them as ss-PCMs that store and release energy via crystallographic structure/order−disorder transformations [72].

Thermally induced SSPT via mechanical molecular motion can mediate intermolecular interaction of chromophores that serve as a visual indication of the process. Wight et al. described colorimetric switching between two differently colored polymorph forms of monoalkoxynaphthalene-naphthalimide donor-acceptor dyads [201]. Upon heating, the orange form of alkyl chain layers became disordered, which facilitated lateral diffusion of dyads within the layer and corresponding dyad exchange from a head-to-head stacking geometry (orange) to a head-to-tail stacking geometry (yellow). This transition involved a nucleation and growth due to a faster cooperative wavefront mechanism during the transition. The fastest moving of the wavefronts corresponded to a non-conventional C–H···O hydrogen bond network of dyad molecules in adjacent stacks that enabled a transition with cooperative character to proceed within the layers of orange crystals. The orange-to-yellow transition was triggered at a temperature that is very close to the temperature at which the orange and yellow forms exchange, while being lower than the melting temperature of the original orange, or final yellow, solids.

5.3 Thermoacoustic Micro-Transducers and Nanomechanical Resonators

Recently, a particular interest was attracted to thermoelastic phenomena where a steady-state thermal bias provides spontaneous long-wave vibrations of a nanomechanical system, i.e., a phenomenon related to the thermoacoustic one. The first numerical results showed that non-Fourier heat transport can yield spontaneous excitation of low frequency mechanical oscillations in the form of transverse acoustic waves in carbon nanotubes [202], graphene [203], 2D hetero-structures [204,205], and graded nanowires [206]. Zheng et al. [207] showed that the frequency of the wave (low frequency phonon) in a graphene nanoribbon (GNR) would decrease and the amplitude of vibration would increase with the increasing

length of GNR. The thinnest known hexagonal boron nitride resonator nano-sheet with ~6.7 nm thickness vibrating at very high frequencies (~5 to ~70 MHz) was demonstrated by Zheng et al. [208]. Shiri et al. [209] observed conversion of heat to mechanical vibration in a symmetrically-divided GNR at room temperature, where the mechanism behind heat-to-vibration conversion was due to the enhancement of the Umklapp process rate which creates a number of low frequency phonons with frequencies from tens of GHz to tens of THz. This mechanism was explained by that the increasing heat flux or, equivalently, temperature gradient, excites high momentum and high energy phonons at the boundary of the Brillouin zone, whereas the high number of phonons as well as the high number of branches due to zone folding increases the available space for phonon scattering.

Application of graphene for development of MEMS, particularly, thermoacoustic transducers at the micro-scale, has been reported recently [210–212], where thermoacoustic sound was generated using a laser. Advantages of graphene are due to its specific properties such as flexibility, multifunctionality, wide operation range of frequencies (up to 1 MHz). For optical transduction applications, however, the high transparency of graphene is disadvantage, but it was proposed that micrometer-wide graphene optical microphones made with assistance of reflective silver coatings or by using thicker GO films can perform similarly or even better than centimeter-scale conventional microphones [213].

Generation of continuous sound was demonstrated in GO sponges and aerogels due to their very efficient light absorption, high porosity and low density. Advantage of GO sponges used as a transducer for LED-driven photothermal sound generation is that these have the photoacoustic performance independent on the wavelength due to the wideband absorption of the sponges [214]. Graphene was used as a remotely excited actuator to enhance the contrast in photoacoustic tomography, where the absorbing contrast injected into the subject was thermally excited by NIR light that better penetrates skin and other tissues with a pulse mode, which resulted in the transient thermoacoustic response of the contrast agent and emission of ultrasound that could be detected using an acoustic sensor [215]. Lalwani et al. [216] demonstrated that GO nanoribbons and nanoplatelets are able to produce photoacoustic and remote thermoacoustic transduction, where a 5–10 fold increase in the photoacoustic response was obtained compared to the response without GO. Moon et al. [217] compared pristine gold nanorods and gold nanorods coated with reduced graphene oxide in order to increase the IR absorbance and photoacoustic performance as a contrasting agent; as a result, an approximately twofold increase in the photoacoustic signal for the rGO coated nanorods and their increased stability upon a 5 min radiation was obtained.

Another trend is the development of metamaterials that assist absorption of IR radiation and its subsequent transduction to mechanical vibrations [218]. In this field, graphene has also attracted attention for its tunable permittivity from the visible to far-infrared region via chemical doping or electrostatic voltage [219]. For example, tunable broadband metamaterial perfect absorbers (BMMPAs) based on graphene disks operating in the mid-infrared region have been demonstrated (Fig. 10a), which had an extended bandwidth of 6.9 THz with more than 80% absorptivity and a full width at half maximum bandwidth of 10.1 THz when the Fermi energy of graphene was 0.1 eV [219]. To further enhance the absorption of graphene materials, different methods have been applied, such as development of graphene-nanovoid arrays [220], exploiting the quantum dots near graphene [221], and plasmonic effect [222,223]. In response to extremely broad frequency range of optical absorption, BMMPA can generate mechanical resonances with other advantages, such as very low oscillation threshold pump power, a broad frequency range of mechanical oscillations (with bandwidth over ~4 THz [224]), and a low Q-factor.

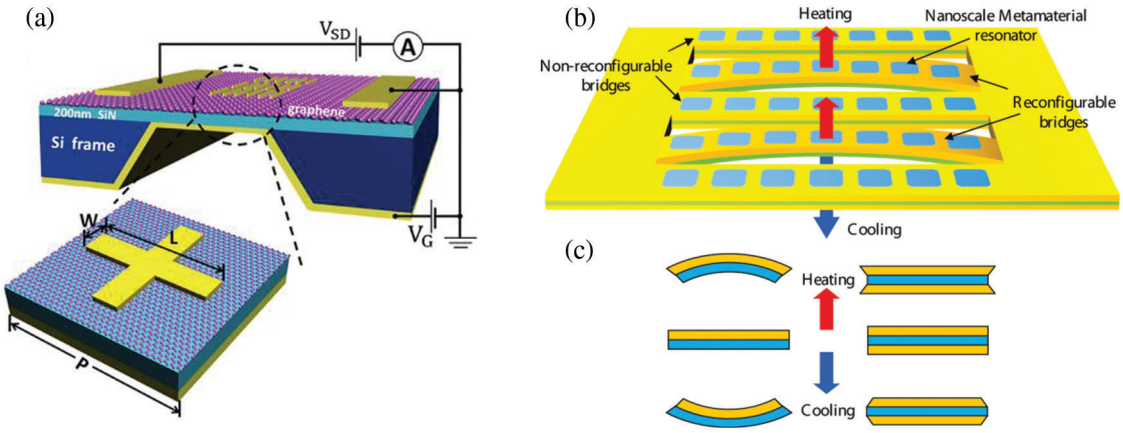

Figure 10: (a) The schematic of the graphene metamaterial perfect absorber and the unit cell of the metamaterial arrays with the golden strips of size of $L = 1.25$ μm and $W = 0.3$ μm. The tunable reflectance can be achieved by back-gating of graphene between the Si_3N_4 membrane and the metasurface. Reprinted from [225] under the Creative Commons Attribution (CC BY) license (http://creativecommons.org/licenses/by/4.0/). Copyright 2019 by the Author(s). Licensee MDPI, Basel, Switzerland. (b) Thermally tunable metamaterial support structure consisting of alternating reconfigurable and nonreconfigurable bimaterial bridges. (c) Bilayered support beams consisting of materials with large (orange, e.g., gold) and small (blue, e.g., silicon nitride) thermal expansion coefficients will bend in response to temperature changes, while bending is inhibited for a symmetric layer sequence. Reprinted with permission from [226]. Copyright 2011 American Chemical Society

5.4 Plasmomechanical Systems

Synergy of plasmonics and mechanics at the nanoscale level yields an emergent field of research called plasmomechanics. Plasmomechanical systems have attracted considerable interest as they can provide fine control of mechanical motion by the optical field of metallic nanostructures that confine light beyond diffraction limit [227–231]. The mechanism of conversion of plasmon field energy into mechanical energy can be understood using the principles of functioning of an optical tweezer. Optical tweezer effect originates from the light refraction passing through a small particle, where the photon momentum is proportional to its energy and therefore it can vary within the laser beam cross-section (Fig. 11). In more detail, when a laser beam passes through a particle, it experiences refraction and alters its momentum, respectively. Due to the momentum conservation of the system, the particle undergoes an equal and opposite momentum change, i.e., a reaction force. The total forces experienced by the particle in most experimental settings, consist of a scattering force and a gradient force [232]. The scattering force is due to the light beam scattering by the surface of the object. This scattering produces a net momentum transfer from the light photons to the object and causes the particle to be pushed towards the beam propagation. The gradient force results from the inhomogeneous intensity profile of the laser beam which acts as an attractive force, drawing the particle towards the region with a greater light intensity (Fig. 11). The gradient force can be expressed via non-uniform electric field $\boldsymbol{E}$ as follows [233]:

$$\langle F \rangle \sim \alpha \nabla \boldsymbol{E}^2 \tag{3}$$

where α is the dipolar polarizability of the particle under consideration.

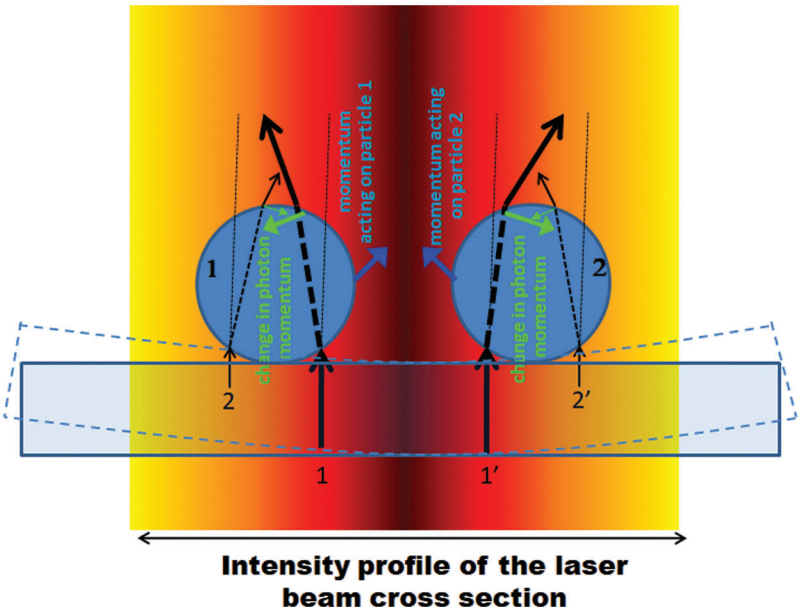

Figure 11: Illustration of the plasmomechanical effect: generation of attraction forces between two nanoparticles attached to a substrate as a result of inhomogeneous local field distribution from the light irradiation (black to yellow colors code decreasing intensity), which leads to mechanical bending of the substrate itself. Shown are the rays (1, 2, 1', 2') of different intensity that experience refraction at particles 1 and 2

Therefore, two nanoparticles separated by the distance that is far less than the light wavelength, will experience attraction towards the region possessing a greater light intensity and thus render mechanical strain on the substrate they are attached to (Fig. 11). In case when the particles are metallic nanoobjects, the gradient force can be greatly enhanced by resonant increment of the electric field due to exciting plasmon fields. Also, the gradient force can be increased by orders of magnitude when employing different kinds of exotic photonic materials such as metamaterials, photonic crystals, and evanescently coupled waveguides [231,234].

Another aspect of plasmomechanical systems is that the incident light in the metamaterial structures that contain plasmonic nanoparticles can be efficiently converted into thermal energy via light trapping-induced localized heating effect [235]. The generated heat causes an increased temperature which can be converted to mechanical actuation of a bilayer structure with different thermal expansion coefficients of the two constituent materials, leading to its bending in response to this temperature increment [12]. Cubukcu and co-workers fabricated a bilayer membrane based on gold-SiN and containing an array of polarization-independent cross-shaped plasmonic nanoslots and a metal backreflector, which efficiently absorbed a continuous-wave 1550 nm laser beam and converted it into heat [224]. The heated membrane then experienced deflection due to the plasmomechanical coupling (Figs. 10b and 10c). This effect was due to dynamic modulation of the total absorbance A, because the absorbance is tuned by δA due to the changes in the absorber gap originating from the natural oscillation of the membrane with amplitude δx. As δA varies between positive and negative values, this change leads to a dynamic modulation on the thermal expansion of the membrane. As a result, a low-power optical pumping at 210 μW yielded a deviation in effective temperature of the mechanical mode from room temperature by as much as 48 K [224].

There are various applications of plasmomechanical systems. First, nanomechanical plasmomechanical resonators are highly sensitive as sensors of minute forces, displacements, masses, heat power, and even quantum information, and are suitable for biomedical diagnosis as well [220,236]. For example, Kosaka and co-workers developed a sandwich assay that combined mechanical and plasmonic transduction for detection of ultra small concentrations of cancer biomarkers in serum [237]. Yi et al. [13] designed a plasmo-thermomechanical IR detector (Plas-MIRD) built by integrating plasmonic nanoantenna absorbers with nano-mechanical structures where the nanoslot antenna absorber was capable of confining the IR light in the slot region. The thermally induced mechanical deflection in the Plas-MIRD could be optically read out through a fiber optic based interferometer, which allowed one to estimate the absorbed infrared power through its noise equivalent power with a density as small as several units of $pW/Hz^{1/2}$. Hu et al. [238] showed that a weak-excitation plasmomechanical strong coupling can be realized in a system consisting of two cuboid-shaped metal nanoparticles, which could potentially offer a nanoscale testbed for quantum experiments in strong coupling regimes and which could further enrich the toolbox for sensing and precise measurements at the molecular scale. Second, plasmomechanical systems can be used to spatially map the displacement modes of a vibrating nanomechanical system with a resolution exceeding the diffraction limit [239]. For example, mechano-optical plasmonic coupling was used for design of a nano-antenna for spatiotemporal temperature mapping with the precise resolution of local temperature in real time, where the aligned plasmonic nanostrips indicated the ambient temperature and the bending ones the elevated temperature, respectively [12].

5.5 Optothermal Walkers

Light-induced mechanical motion of single molecules and nano-objects, which constitutes the basis of light-driven artificial molecular machines, is an active concept developed during the last decades [240–243], which resulted in awarding the Nobel Prize in Chemistry for 2016 to J. Pierre Sauvage, J. Fraser Stoddart, and B. Feringa for their achievements in the design and synthesis of molecular machines [244]. This idea was also inspired by the fact that photochromic molecular materials are able for relatively long-range photoinduced mass flow [245].

Some molecular engines enable the directional movements or locomotion upon absorption of electromagnetic energy. The driving forces for molecular motors at the nanoscale can be divided into those owing to electronic excitation and due to temperature changes, which again can be referred to as photonic and thermal devices, respectively (see Section 3).

Photoisomerization can be translated into the motion of a molecule, both rotary and linear. Recently developed light-driven rotary motors indicated 360° unidirectional rotary motion due to the interplay between point and helical chirality [246]. Filatov et al. [247] demonstrated by computational design a new family of light-driven molecular rotary motors which utilize the fulgide motif to perform pure unidirectional axial rotation of the rotor moiety with high quantum efficiency and ultrafast dynamics (200–300 fs) of its successive photoisomerization steps. Attachment of a biphenol moiety to the rotor, which serves as a “handle” to alter the rotary behavior of the motor through non-covalent substrate binding, was developed as a strategy to decrease the rotation of light-driven molecular motors [248]. Hou et al. [249] demonstrated rotary motors that are able to convert light energy into reversible helical motion, where a specific photochemically-driven motion occurred owing to a dual function of the molecular motor which was able to act both as a chiral dopant and unidirectional rotor that amplifies molecular motion into a controlled and reversible left- or right-handed macroscopic twisting movement.

A linear motion of the photonic molecular motors can be realized by two subsequent photoisomerization steps which push a molecule by a certain distance. Synthesis of molecular motors of the third generation, which represent a combination of two parallel motors with opposite helicity, opens up a new perspective in this direction [250]. Mesostructures of the third generation contain a pseudo-asymmetry center, in respect to which one rotor rotates clockwise and the other anti-clockwise, which gives rise to the unidirectional rotary motion of the parallel rotors [251]. A particular application of such unidirectional translation was recently demonstrated with a nanocar for locomotion and cargo transport [252].

However, true thermal devices were realized through triggering device actuation by the neat thermal energy [253,254]. Cheng et al. [255] reported fabrication of different types of thermomechanical actuators showing a motion in space in response to combination of different stimulus such as moisture and IR radiation which can control water adsorption and desorption in the GO samples, respectively. Several devices such as "smart fingers", a temperature-triggered three feet "crane", a bipedal "reptile", a "rectangle" walker, and a four-legged walker have been demonstrated. A three-finger responsive device was composed of GO strips with a width of 5 mm, where the motion of each finger was controlled by IR irradiation, with simultaneous detection of the corresponding deformation by the built-in laser-writing rGO sensor in the real time in the form of a peak of the electric signal (Fig. 12). The "rectangle" walker was able to crawl on a special ratchet substrate through the repetitive bending and straight deformation walking step by step, triggered by the alternation of the IR radiation on/off switching. The moving rate was about 2 mm per step, and the device, while performing three cycles, could walk a total of 6 mm (Fig. 12). In the three feet "crane", the increase in temperature to around 80°C led to bending the crane's legs followed by their erection, respectively (Fig. 12). In the four-legged walker, the increase in humidity level led to bending all the legs that drove the whole device forward, whereas exposure to IR light recovered the legs to the initial state. Thus, with alternation of the surrounding stimulus, the device could move step by step forward on the smooth glass substrate.

An optically reconfigurable sequential locomotion of light-fueled microwalker using dye-doped LCN actuator triggered by NIR light (980 nm, 4.5 Wcm^{-2}) was demonstrated by Jiang et al. [99]. In this device, the thermal-fueled locomotion process was promoted owing to the strong absorption of the NIR dye loaded into the LCN matrix, which provided a light-induced rapid heating to 70°C within 6 s only.

Thermomechanical deformation of polymer strips can also be used as an intermediate trigger to control a mechanical motion of a larger device. For example, Sarkisiv et al. demonstrated a mechanical clock in the form of a wheel whose stepwise motion was triggered by deformation of polyvinylidene fluoride strips initiated by periodic exposure to IR laser beam with a power of only a few milliwatts [256,257].

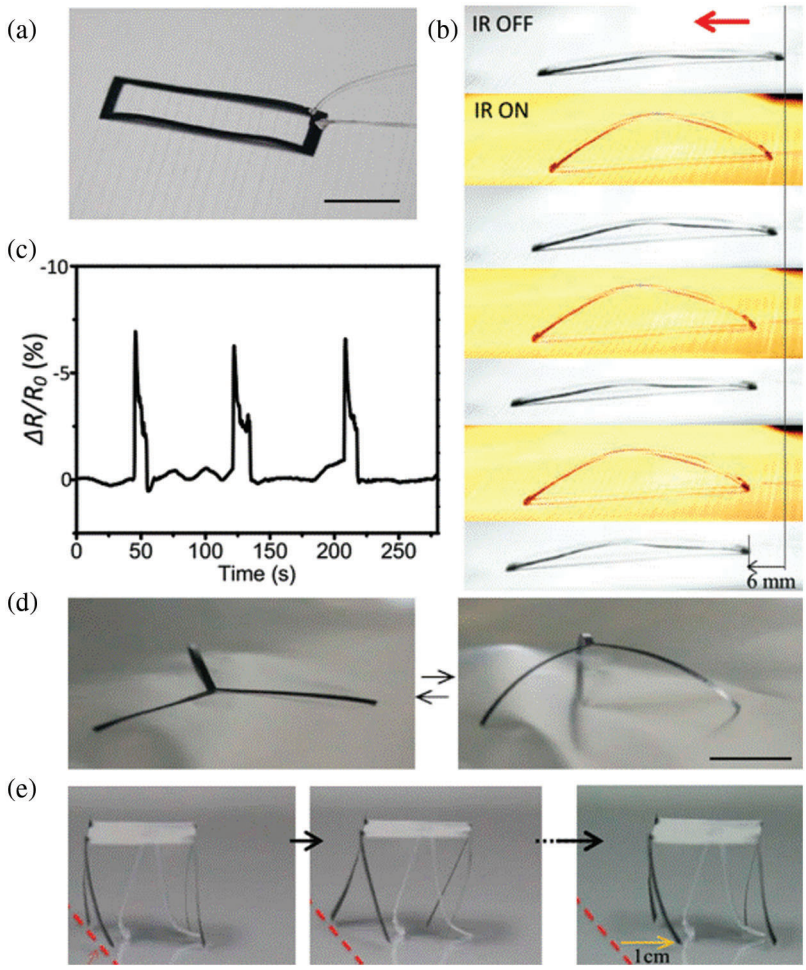

Figure 12: (a) Photograph of a "rectangle" walker on a ratchet paper. (b) Series of photographs of the "rectangle" walker crawling on the ratchet paper in response to on/off states of the IR light. (c) Detected current changes along with the "rectangle" walker's steps shown in (b). (d) Deformation of a three feet "crane" under temperature change. Left: initial state at room temperature. Right: lifting state at 80°C. (e) Series of photographs of a four-legged walker moving forward on a smooth glass. Scale bars: (a, d) 1 cm. Reprinted with permission from reference [255]. Copyright 2016, American Chemical Society

6 Conclusions and Outlook

Thermomechanical engines that convert electromagnetic energy to mechanical work represent a reasonable alternative to devices that convert electromagnetic energy directly to electricity. First, thermomechanical energy converters operate in the lower-energy domain of electromagnetic waves in regard to the UV-visible spectrum, i.e., in the NIR-IR region, where the conventional solar cells usually have poor efficiency or are totally silent. Although many thermomechanical engines have also low power conversion efficiency, of the order of few percents, nevertheless, the thermal noise, which represents a serious drawback for photonic devices, does not affect the performance but instead serves as a useful energy "fuel" for the thermal devices. As a result, thermomechanical engines can harvest the low-grade thermal energy which is considered as thermal waste and which otherwise contributes to the negative climate changes. Remarkably, the sources of the low-grade thermal energy can be found everywhere, i.e., these originate from the direct solar radiation, outgoing terrestrial radiation, waste heat due to combustion

processes, heat-emitting electrical and electronic devices, decay of radioactive isotopes, human and animal body heat, heat from organic putrefaction and fermentation, etc.

Another advantage of thermomechanical energy converters is their variety in terms of different principles of operation and construction features, which can be adjusted for specific needs of thermal energy collection and conversion at macro-, micro-, or nano-scale, and which therefore can find specific niche applications.

Finally, many thermomechanical engines are made of relatively cheap materials and therefore can compete in terms of efficiency/cost ratio with other energy converters. It would be incorrect to compare energy production costs between different devices that convert renewable energy into electricity and thermal energy into mechanical work, respectively, as these are measured in qualitatively different terms. However, in the first approximation, solar thermal and geothermal energy converters can be taken as those that involve intermediate thermomechanical processes. Comparing renewables, the energy production costs from solar thermal (6–15 cents/kWh) are cheaper than that from solar photovoltaics (20–30 cents/kWh), while geothermal energy costs (5–8 cents/kWh) are comparable with costs of biomass, wind, and large hydropower production [258].

To compare different groups of thermomechanical energy converters, besides estimates in terms of compactness and smartness (see Fig. 1), other criteria can be applied, such as efficiency, output power, material costs and material abundance [259]. In the first group that represents macroscopic devices, rather reasonable efficiencies above 30% for thermoacoustic engines, and above 70% for hydride heat engines can be achieved; however, specific energy and output power of these devices is still low. Moreover, some devices, such as TMG, SMA, and hydride heat engines involve rare metals for their manufacturing, which increases their cost. A mere drawback of the other groups, i.e., the thermoelastic and emergent engines, is still their low efficiency, normally below 2% (Table 1). However, some devices of the latter group demonstrate increasing power density of tens of watts per gram, which makes them viable for application as micro- and nano-actuators, where specific architecture is required, thus opening up avenues towards soft, autonomous, and small-scale devices. Moreover, inexpensive and renewable materials can be used for their production.

Because of the usually low specific energy produced by thermomechanical energy converters they cannot compete with conventional engines based, for example, on fuel feeding, whose generated specific energy is of the order of tens of kJ/g. Instead, they can be used, for example, as controlling devices, switches, valves, trackers, counting mechanisms and similar, where modest mechanical efforts are needed. Besides direct conversion of thermal energy to mechanical work, thermomechanical energy converters can also operate as energy storage devices due to resilience, i.e., the ability of a material to absorb energy when it is deformed elastically, and release that energy upon unloading, where deformation is induced by heating. In this direction, there is a great potential for elastic materials, such as nylon, rubber band, etc., whose stored energy density is several J/g [260], whereas conventional metals like aluminum and steel possess an order lower stored energy density. Even a more interesting trend in this direction is the use of materials such as photo-isomers that are able to change conformation upon heat exposure, which provides a great opportunity for development of energy storage devices [156,157]. Particularly, combination of the photo-isomer and MOF yields an order higher value of the stored energy density compared to polymers (Table 1).

The above advantages of thermomechanical energy converters can provide exciting opportunities for future applications. The progress in engineering and miniaturizing devices based on the photo/thermo-driven mechanical motions leads to the emerging technologies for photo-fueled miniature flying machines, remotely controlled micro-optomechanical systems, light-controlled microfluidic valves, linear and torsional actuators, chemically activated thermal actuators, solar trackers, vibration dampers,

biomedical actuators, energy harvesting devices, waste heat recovery devices, actuated fitting garment and textiles, and so on. The recent and ongoing trends in this direction are expected to bring new exciting findings that will be widely used in the energy sector in the near future.

Funding Statement: The author is grateful to the Ministry of Education and Sciences of Ukraine (https://mon.gov.ua) for continuing support (Project # M/66-2022).

Conflicts of Interest: The author declares that he has no conflicts of interest to report regarding the present study.

References

1. Forman, C., Muritala, I. K., Pardemann, R., Meyer, B. (2016). Estimating the global waste heat potential. *Renewable and Sustainable Energy Reviews, 57,* 1568–1579. DOI 10.1016/j.rser.2015.12.192.
2. Dimitriev, O. P. (2019). Harvesting of the infrared energy: Direct collection, up-conversion, and storage. *Semiconductor Physics, Quantum Electronics & Optoelectronics, 22(4),* 457–469. DOI 10.15407/spqeo.
3. Norton, P. (1999). HgCdTe infrared detectors. *Proceedings of the Sixth International Symposium on Long Wavelength Infrared Detectors and Arrays: Physics and Applications*, vol. 98, no. 21, pp. 49. Boston, MA: The Electrochemical Society.
4. Sargent, E. H. (2008). Solar cells, photodetectors, and optical sources from infrared colloidal quantum dots. *Advanced Materials, 20(20),* 3958–3964. DOI 10.1002/adma.200801153.
5. Orr, B., Akbarzadeh, A., Mochizuki, M., Singh, R. (2016). A review of car waste heat recovery systems utilising thermoelectric generators and heat pipes. *Applied Thermal Engineering, 101,* 490–495. DOI 10.1016/j.applthermaleng.2015.10.081.
6. Kanygin, M. A., Bahreyni, B. (2021). Self-powered integrated opto-electro-mechanical nano-actuators. *Nano Energy, 88,* 106280. DOI 10.1016/j.nanoen.2021.106280.
7. Geetha, T., Balaji, J., Dinesh, M., Dhivakar, S. (2021). Things and everything: Internet of nano-things future growth trends. *International Journal of Computer Science Engineering Techniques, 6(2),* 1–11.
8. Zakharov, D., Lebedev, G., Irzhak, A., Afonina, V., Mashirov, A. et al. (2012). Submicron-sized actuators based on enhanced shape memory composite material fabricated by FIB-CVD. *Smart Materials and Structures, 21(5),* 052001. DOI 10.1088/0964-1726/21/5/052001.
9. Gratowski, S. V., Koledov, V., Shavrov, V., Petrenko, S., Irzhak, A. et al. (2018). Advanced system for nanofabrication and nanomanipulation based on shape memory alloy. In: *Frontiers in materials processing, applications, research and technology*, pp. 135–154. Singapore: Springer.
10. Barillé, R., Ortyl, E., Zielinska, S. (2019). Azobenzene polymers as photoactive materials for shape changes of micro/nano-objects. In: *Photoactive functional soft materials: Preparation, properties, and applications,* pp. 389–411. Kent, OH: Wiley-VCH Verlag GmbH & Co.
11. Eltaher, M. A., Agwa, M. A., Mahmoud, F. F. (2016). Nanobeam sensor for measuring a zeptogram mass. *International Journal of Mechanics and Materials in Design, 12(2),* 211–221. DOI 10.1007/s10999-015-9302-5.
12. Liu, Y., Park, Y., Lee, S. E. (2016). Thermo-responsive mechano-optical plasmonic nano-antenna. *Applied Physics Letters, 109(1),* 013109. DOI 10.1063/1.4954907.
13. Yi, F., Zhu, H., Reed, J. C., Cubukcu, E. (2013). Plasmonically enhanced thermomechanical detection of infrared radiation. *Nano Letters, 13(4),* 1638–1643. DOI 10.1021/nl400087b.
14. Chandel, V. S., Wang, G., Talha, M. (2020). Advances in modelling and analysis of nano structures: A review. *Nanotechnology Reviews, 9(1),* 230–258. DOI 10.1515/ntrev-2020-0020.
15. Gotti, C., Sensini, A., Zucchelli, A., Carloni, R., Focarete, M. L. (2020). Hierarchical fibrous structures for muscle-inspired soft-actuators: A review. *Applied Materials Today, 20,* 100772. DOI 10.1016/j.apmt.2020.100772.
16. Zheng, Q., Xu, C., Jiang, Z., Zhu, M., Chen, C. et al. (2021). Smart actuators based on external stimulus response. *Frontiers in Chemistry, 9,* 650358. DOI 10.3389/fchem.2021.650358.

17. Zhang, W., Wang, L., Sun, K., Luo, T., Yu, Z. et al. (2018). Graphene-based janus film with improved sensitive response capacity for smart actuators. *Sensors and Actuators B: Chemical, 268,* 421–429. DOI 10.1016/j.snb.2018.04.104.
18. Hassani, F. A., Shi, Q., Wen, F., He, T., Haroun, A. et al. (2020). Smart materials for smart healthcare–moving from sensors and actuators to self-sustained nanoenergy nanosystems. *Smart Materials in Medicine, 1,* 92–124. DOI 10.1016/j.smaim.2020.07.005.
19. Chen, S., Pang, Y., Yuan, H., Tan, X., Cao, C. (2020). Smart soft actuators and grippers enabled by self-powered tribo-skins. *Advanced Materials Technologies, 5(4),* 1901075. DOI 10.1002/admt.201901075.
20. Swift, G. W. (1988). Thermoacoustic engines. *The Journal of the Acoustical Society of America, 84(4),* 1145–1180. DOI 10.1121/1.396617.
21. Tijani, H., Spoelstra, S., Poignand, G. (2008). Study of a thermoacoustic-stirling engine. *The Journal of the Acoustical Society of America, 123(5),* 3541. DOI 10.1121/1.2934525.
22. Backhaus, S., Swift, G. W. (1999). A thermoacoustic stirling heat engine. *Nature, 399(6734),* 335–338. DOI 10.1038/20624.
23. Serry, M., Aziz, A. A., Rahman, E. A., Sedky, S. (2009). A new approach for MEMS power generation based on thermoacoustic heat engine. *The 9th International Workshop on Micro and Nanotechnology for Power Generation and Energy Conversion Applications, Power MEMS*, pp. 526–529. Maryland, USA.
24. Chen, L., Feng, H., Ge, Y. (2020). Power and efficiency optimization for open combined regenerative brayton and inverse brayton cycles with regeneration before the inverse cycle. *Entropy, 22(6),* 677. DOI 10.3390/e22060677.
25. Tijani, M. E. H., Spoelstra, S. (2011). A high performance thermoacoustic engine. *Journal of Applied Physics, 110(9),* 093519. DOI 10.1063/1.3658872.
26. Jung, S., Matveev, K. I. (2010). Study of a small-scale standing-wave thermoacoustic engine. *Proceedings of the Institution of Mechanical Engineers, Part C: Journal of Mechanical Engineering Science, 224(1),* 133–141. DOI 10.1243/09544062JMES1594.
27. Saechan, P., Jaworski, A. J. (2019). Numerical studies of co-axial travelling-wave thermoacoustic cooler powered by standing-wave thermoacoustic engine. *Renewable Energy, 139,* 600–610. DOI 10.1016/j.renene.2019.02.059.
28. Wang, X., Xu, J., Wu, Z., Luo, E. (2022). A thermoacoustic refrigerator with multiple-bypass expansion cooling configuration for natural gas liquefaction. *Applied Energy, 313,* 118780. DOI 10.1016/j.apenergy.2022.118780.
29. Saechan, P., Jaworski, A. J. (2018). Thermoacoustic cooler to meet medical storage needs of rural communities in developing countries. *Thermal Science and Engineering Progress, 7,* 164–175. DOI 10.1016/j.tsep.2018.05.001.
30. Xu, J., Hu, J., Luo, E., Hu, J., Zhang, L. et al. (2022). Numerical study on a heat-driven piston-coupled multi-stage thermoacoustic-stirling cooler. *Applied Energy, 305,* 117904. DOI 10.1016/j.apenergy.2021.117904.
31. Otsuka, K., Wayman, C. M. (1999). Mechanisms of shape memory effect and superelasticity. In: *Shape memory materials*, pp. 27–48. Cambridge, UK: Cambridge University Press.
32. Josephine, S., Ruth, D., Glory Rebekah, S. D. (2020). Shape memory alloys. In: *Alloy materials and their allied applications*, pp. 213–223. Beverly, MA: Scrivener Publishing. DOI 10.1002/9781119654919.
33. Farber, E., Zhu, J. N., Popovich, A., Popovich, V. (2020). A review of NiTi shape memory alloy as a smart material produced by additive manufacturing. *Materials Today: Proceedings, 30,* 761–767.
34. Madden, J. D., Vandesteeg, N. A., Anquetil, P. A., Madden, P. G., Takshi, A. et al. (2004). Artificial muscle technology: Physical principles and naval prospects. *IEEE Journal of Oceanic Engineering, 29(3),* 706–728. DOI 10.1109/JOE.2004.833135.
35. Percy, S., Knight, C., McGarry, S., Post, A., Moore, T. et al. (2014). Other thermomechanical heat engines. In: *Thermal energy harvesting for application at MEMS scale*, pp. 25–39. New York: Springer.
36. Stöckel, D. (1995). The shape memory effect-phenomenon, alloys and applications. *Proceedings: Shape Memory Alloys for Power Systems EPRI, 1,* 1–13.
37. Mirvakili, S. M., Hunter, I. W. (2018). Artificial muscles: Mechanisms, applications, and challenges. *Advanced Materials, 30(6),* 1704407. DOI 10.1002/adma.201704407.

38. Kumar, P., Kishore, R. A., Maurya, D., Stewart, C. J., Mirzaeifar, R. et al. (2019). Shape memory alloy engine for high efficiency low-temperature gradient thermal to electrical conversion. *Applied Energy, 251,* 113277. DOI 10.1016/j.apenergy.2019.05.080.
39. Abubakar, R. A., Wang, F., Wang, L. (2020). A review on nitinol shape memory alloy heat engines. *Smart Materials and Structures, 30(1),* 013001. DOI 10.1088/1361-665X/abc6b8.
40. Zare, M., Prabhakaran, M. P., Parvin, N., Ramakrishna, S. (2019). Thermally-induced two-way shape memory polymers: Mechanisms, structures, and applications. *Chemical Engineering Journal, 374,* 706–720. DOI 10.1016/j.cej.2019.05.167.
41. Xia, Y., He, Y., Zhang, F., Liu, Y., Leng, J. (2021). A review of shape memory polymers and composites: Mechanisms, materials, and applications. *Advanced Materials, 33(6),* 2000713. DOI 10.1002/adma.202000713.
42. Herath, M., Epaarachchi, J., Islam, M., Fang, L., Leng, J. (2020). Light activated shape memory polymers and composites: A review. *European Polymer Journal, 136,* 109912. DOI 10.1016/j.eurpolymj.2020.109912.
43. Jani, J. M., Leary, M., Subic, A., Gibson, M. A. (2014). A review of shape memory alloy research, applications and opportunities. *Materials & Design, 56,* 1078–1113. DOI 10.1016/j.matdes.2013.11.084.
44. Behl, M., Zotzmann, J., Lendlein, A. (2009). Shape-memory polymers and shape-changing polymers. In: *Shape-memory polymers*, pp. 1–40. Heidelberg: Springer. DOI 10.1007/978-3-642-12359-7.
45. Leng, J., Du, S. (2010). *Shape-memory polymers and multifunctional composites*. USA: CRC Press.
46. Bastiaansen, C. W. M., Meyer, H. E. H., Lemstra, P. J. (1990). Memory effects in polyethylenes: Influence of processing and crystallization history. *Polymer, 31(8),* 1435–1440. DOI 10.1016/0032-3861(90)90147-Q.
47. Mather, P. T., Luo, X., Rousseau, I. A. (2009). Shape memory polymer research. *Annual Review of Materials Research, 39(1),* 445–471. DOI 10.1146/annurev-matsci-082908-145419.
48. Lendlein, A., Gould, O. E. (2019). Reprogrammable recovery and actuation behaviour of shape-memory polymers. *Nature Reviews Materials, 4(2),* 116–133. DOI 10.1038/s41578-018-0078-8.
49. Zhang, H., Zhao, Y. (2013). Polymers with dual light-triggered functions of shape memory and healing using gold nanoparticles. *ACS Applied Materials & Interfaces, 5(24),* 13069–13075. DOI 10.1021/am404087q.
50. Guo, Q., Bishop, C. J., Meyer, R. A., Wilson, D. R., Olasov, L. et al. (2018). Entanglement-based thermoplastic shape memory polymeric particles with photothermal actuation for biomedical applications. *ACS Applied Materials & Interfaces, 10(16),* 13333–13341. DOI 10.1021/acsami.8b01582.
51. Toncheva, A., Khelifa, F., Paint, Y., Voue, M., Lambert, P. et al. (2018). Fast IR-actuated shape-memory polymers using in situ silver nanoparticle-grafted cellulose nanocrystals. *ACS Applied Materials & Interfaces, 10(35),* 29933–29942. DOI 10.1021/acsami.8b10159.
52. Fang, L., Chen, S., Fang, T., Fang, J., Lu, C. et al. (2017). Shape-memory polymer composites selectively triggered by near-infrared light of two certain wavelengths and their applications at macro-/microscale. *Composites Science and Technology, 138,* 106–116. DOI 10.1016/j.compscitech.2016.11.018.
53. Wu, S., Li, W., Zhou, W., Zhan, Y., Hu, C. et al. (2018). Large-scale one-step synthesis of carbon dots from yeast extract powder and construction of carbon dots/PVA fluorescent shape memory material. *Advanced Optical Materials, 6(7),* 1701150. DOI 10.1002/adom.201701150.
54. Yu, K., Liu, Y., Leng, J. (2014). Shape memory polymer/CNT composites and their microwave induced shape memory behaviors. *RSC Advances, 4(6),* 2961–2968. DOI 10.1039/C3RA43258K.
55. Kalita, H., Karak, N. (2013). Hyperbranched polyurethane/Fe_3O_4 nanoparticles decorated multiwalled carbon nanotube thermosetting nanocomposites as microwave actuated shape memory materials. *Journal of Materials Research, 28(16),* 2132–2141. DOI 10.1557/jmr.2013.213.
56. Li, S. T., Jin, X. Z., Shao, Y. W., Qi, X. D., Yang, J. H. et al. (2019). Gold nanoparticle/reduced graphene oxide hybrids for fast light-actuated shape memory polymers with enhanced photothermal conversion and mechanical stiffness. *European Polymer Journal, 116,* 302–310. DOI 10.1016/j.eurpolymj.2019.04.029.
57. Cui, X., Chen, J., Zhu, Y., Jiang, W. (2020). Natural sunlight-actuated shape memory materials with reversible shape change and self-healing abilities based on carbon nanotubes filled conductive polymer composites. *Chemical Engineering Journal, 382,* 122823. DOI 10.1016/j.cej.2019.122823.

58. Zhou, Y., Tan, J., Chong, D., Wan, X., Zhang, J. (2019). Rapid near-infrared light responsive shape memory polymer hybrids and novel chiral actuators based on photothermal W18O49 nanowires. *Advanced Functional Materials, 29(33),* 1901202. DOI 10.1002/adfm.201901202.
59. Qi, X., Xu, E., Jia, M., Zhang, J., Zhang, L. et al. (2021). Bio-based, self-crosslinkable eucommia ulmoides gum/silica hybrids with body temperature triggering shape memory capability. *Macromolecular Materials and Engineering, 306(11),* 2100370. DOI 10.1002/mame.202100370.
60. Yakacki, C. M., Gall, K. (2009). Shape-memory polymers for biomedical applications. *Shape-Memory Polymers,* 147–175. DOI 10.1007/978-3-642-12359-7.
61. Gao, Y., Liu, W., Zhu, S. (2019). Thermoplastic polyolefin elastomer blends for multiple and reversible shape memory polymers. *Industrial & Engineering Chemistry Research, 58(42),* 19495–19502. DOI 10.1021/acs.iecr.9b03979.
62. Kalra, S., Desai, K. P., Naik, H. B., Atrey, M. D. (2015). Theoretical study on standing wave thermoacoustic engine. *Physics Procedia, 67,* 456–461. DOI 10.1016/j.phpro.2015.06.058.
63. Gil, F. J., Planell, J. A. (1999). Thermal efficiencies of NiTiCu shape memory alloys. *Thermochimica Acta, 327(1–2),* 151–154. DOI 10.1016/S0040-6031(98)00607-8.
64. Nikonovas, T., Spessa, A., Doerr, S. H., Clay, G. D., Mezbahuddin, S. (2020). Near-complete loss of fire-resistant primary tropical forest cover in Sumatra and Kalimantan. *Communications Earth & Environment, 1(1),* 1–8. DOI 10.1038/s43247-020-00069-4.
65. Joseph, J., Ohtsuka, M., Miki, H., Kohl, M. (2020). Upscaling of thermomagnetic generators based on Heusler alloy films. *Joule, 4(12),* 2718–2732. DOI 10.1016/j.joule.2020.10.019.
66. Kishore, R. A., Singh, D., Sriramdas, R., Garcia, A. J., Sanghadasa, M. et al. (2020). Linear thermomagnetic energy harvester for low-grade thermal energy harvesting. *Journal of Applied Physics, 127(4),* 044501. DOI 10.1063/1.5124312.
67. Wu, Z., Tan, P., Zhu, P., Cai, W., Chen, B. et al. (2019). Performance analysis of a novel SOFC-HCCI engine hybrid system coupled with metal hydride reactor for H_2 addition by waste heat recovery. *Energy Conversion and Management, 191,* 119–131. DOI 10.1016/j.enconman.2019.04.016.
68. Ajay, M., Maiya, M. P., Srinivasa Murthy, S. (2009). Performance of a metal hydride device for simultaneous heat transformation and refrigeration. *International Journal of Low-Carbon Technologies, 4(2),* 84–95. DOI 10.1093/ijlct/ctp009.
69. Muthukumar, P., Kumar, A., Raju, N. N., Malleswararao, K., Rahman, M. M. (2018). A critical review on design aspects and developmental status of metal hydride based thermal machines. *International Journal of Hydrogen Energy, 43(37),* 17753–17779. DOI 10.1016/j.ijhydene.2018.07.157.
70. Lima, M. D., Li, N., Jung de Andrade, M., Fang, S., Oh, J. et al. (2012). Electrically, chemically, and photonically powered torsional and tensile actuation of hybrid carbon nanotube yarn muscles. *Science, 338(6109),* 928–932. DOI 10.1126/science.1226762.
71. Mirvakili, S. M., Pazukha, A., Sikkema, W., Sinclair, C. W., Spinks, G. M. et al. (2013). Niobium nanowire yarns and their application as artificial muscles. *Advanced Functional Materials, 23(35),* 4311–4316. DOI 10.1002/adfm.201203808.
72. Griffiths, K., Halcovitch, N. R., Griffin, J. M. (2020). Long-term solar energy storage under ambient conditions in a MOF-based solid–solid phase-change material. *Chemistry of Materials, 32(23),* 9925–9936. DOI 10.1021/acs.chemmater.0c02708.
73. Dimitriieva, P., Doroshenko, T., Fedoryak, A., Dimitriev, O. (2022). Thermomechanical properties of artificial muscle based on silicone-carbon fiber composite. *ECS Transactions, 107(1),* 10977. DOI 10.1149/10701.10977ecst.
74. Li, S., Bai, H., Liu, Z., Zhang, X., Huang, C. et al. (2021). Digital light processing of liquid crystal elastomers for self-sensing artificial muscles. *Science Advances, 7(30),* eabg3677. DOI 10.1126/sciadv.abg3677.
75. Haines, C. S., Lima, M. D., Li, N., Spinks, G. M., Foroughi, J. et al. (2014). Artificial muscles from fishing line and sewing thread. *Science, 343(6173),* 868–872. DOI 10.1126/science.1246906.

76. Mehmood, M. U., Kim, Y., Ahmed, R., Lee, J., Chun, W. (2021). Design and operation of a thermomagnetic engine for the exploitation of low-grade thermal energy. *International Journal of Energy Research, 45(10),* 15298–15311. DOI 10.1002/er.6804.
77. Phillips, M. R., Carman, G. P. (2020). Numerical analysis of an active thermomagnetic device for thermal energy harvesting. *Journal of Energy Resources Technology, 142(8),* 082102. DOI 10.1115/1.4046273.
78. Stauss, H. E. (1959). Efficiency of thermomagnetic generator. *Journal of Applied Physics, 30(10),* 1622–1623. DOI 10.1063/1.1735020.
79. Kishore, R. A., Priya, S. (2018). A review on design and performance of thermomagnetic devices. *Renewable and Sustainable Energy Reviews, 81,* 33–44. DOI 10.1016/j.rser.2017.07.035.
80. Chen, H., Ma, Z., Liu, X., Qiao, K., Xie, L. et al. (2022). Evaluation of thermomagnetic generation performance of classic magnetocaloric materials for harvesting low-grade waste heat. *Applied Energy, 306,* 117999. DOI 10.1016/j.apenergy.2021.117999.
81. Joseph, J., Ohtsuka, M., Miki, H., Kohl, M. (2021). Lumped element model for thermomagnetic generators based on magnetic SMA films. *Materials, 14(5),* 1234. DOI 10.3390/ma14051234.
82. Gueltig, M., Wendler, F., Ossmer, H., Ohtsuka, M., Miki, H. et al. (2017). High-performance thermomagnetic generators based on heusler alloy films. *Advanced Energy Materials, 7(5),* 1601879. DOI 10.1002/aenm.201601879.
83. Dzekan, D., Waske, A., Nielsch, K., Fähler, S. (2021). Efficient and affordable thermomagnetic materials for harvesting low grade waste heat. *APL Materials, 9(1),* 011105. DOI 10.1063/5.0033970.
84. Ham, S., Kang, S., Kim, K. J. (2020). A numerical study for performance prediction of a metal hydride thermal energy conversion system elaborating the superadiabatic condition. *Energies, 13(12),* 3095. DOI 10.3390/en13123095.
85. Nyallang Nyamsi, S., Tolj, I., Lototskyy, M. (2019). Metal hydride beds-phase change materials: Dual mode thermal energy storage for medium-high temperature industrial waste heat recovery. *Energies, 12(20),* 3949. DOI 10.3390/en12203949.
86. Mita, I., Horie, K., Hirao, K. (1989). Photochemistry in polymer solids. 9. Photoisomerization of azobenzene in a polycarbonate film. *Macromolecules, 22(2),* 558–563. DOI 10.1021/ma00192a008.
87. Liu, R. S. (2001). Photoisomerization by hula-twist: A fundamental supramolecular photochemical reaction. *Accounts of Chemical Research, 34(7),* 555–562. DOI 10.1021/ar000165c.
88. Zhao, Y., Ikeda, T. (2009). *Smart light-responsive materials: Azobenzene-containing polymers and liquid crystals*. USA: John Wiley & Sons.
89. Irie, M. (2000). Diarylethenes for memories and switches. *Chemical Reviews, 100(5),* 1685–1716. DOI 10.1021/cr980069d.
90. Hampp, N. (2000). Bacteriorhodopsin as a photochromic retinal protein for optical memories. *Chemical Reviews, 100(5),* 1755–1776. DOI 10.1021/cr980072x.
91. Günes, S., Neugebauer, H., Sariciftci, N. S. (2007). Conjugated polymer-based organic solar cells. *Chemical Reviews, 107(4),* 1324–1338. DOI 10.1021/cr050149z.
92. Rus, D., Tolley, M. T. (2015). Design, fabrication and control of soft robots. *Nature, 521(7553),* 467–475. DOI 10.1038/nature14543.
93. Miriyev, A., Stack, K., Lipson, H. (2017). Soft material for soft actuators. *Nature Communications, 8(1),* 1–8. DOI 10.1038/s41467-017-00685-3.
94. Ikeda, T., Mamiya, J. I., Yu, Y. (2007). Photomechanics of liquid-crystalline elastomers and other polymers. *Angewandte Chemie International Edition, 46(4),* 506–528. DOI 10.1002/(ISSN)1521-3773.
95. Oscurato, S. L., Salvatore, M., Maddalena, P., Ambrosio, A. (2018). From nanoscopic to macroscopic photo-driven motion in azobenzene-containing materials. *Nanophotonics, 7(8),* 1387–1422. DOI 10.1515/nanoph-2018-0040.

96. Mahimwalla, Z., Yager, K. G., Mamiya, J. I., Shishido, A., Priimagi, A. et al. (2012). Azobenzene photomechanics: Prospects and potential applications. *Polymer Bulletin, 69(8),* 967–1006. DOI 10.1007/s00289-012-0792-0.
97. Conti, I., Garavelli, M., Orlandi, G. (2008). The different photoisomerization efficiency of azobenzene in the lowest nπ* and ππ* singlets: The role of a phantom state. *Journal of the American Chemical Society, 130(15),* 5216–5230. DOI 10.1021/ja710275e.
98. Merritt, I. C., Jacquemin, D., Vacher, M. (2021). *Cis*→trans photoisomerisation of azobenzene: A fresh theoretical look. *Physical Chemistry Chemical Physics, 23(35),* 19155–19165. DOI 10.1039/D1CP01873F.
99. Jiang, Z. C., Xiao, Y. Y., Tong, X., Zhao, Y. (2019). Selective decrosslinking in liquid crystal polymer actuators for optical reconfiguration of origami and light-fueled locomotion. *Angewandte Chemie, 131(16),* 5386–5391. DOI 10.1002/ange.201900470.
100. Harris, J. D., Moran, M. J., Aprahamian, I. (2018). New molecular switch architectures. *Proceedings of the National Academy of Sciences, 115(38),* 9414–9422. DOI 10.1073/pnas.1714499115.
101. Yamamoto, K., Mutoh, K., Abe, J. (2019). Photo-and electro-driven molecular switching system of aryl-bridged photochromic radical complexes. *The Journal of Physical Chemistry A, 123(10),* 1945–1952. DOI 10.1021/acs.jpca.8b12384.
102. Ma, L., Li, C., Yan, Q., Wang, S., Miao, W. et al. (2020). Unsymmetrical photochromic bithienylethene-bridge tetraphenylethene molecular switches: Synthesis, aggregation-induced emission and information storage. *Chinese Chemical Letters, 31(2),* 361–364. DOI 10.1016/j.cclet.2019.07.040.
103. Marazzi, M., Francés-Monerris, A., Mourer, M., Pasc, A., Monari, A. (2020). Trans-to-*cis* photoisomerization of cyclocurcumin in different environments rationalized by computational photochemistry. *Physical Chemistry Chemical Physics, 22(8),* 4749–4757. DOI 10.1039/C9CP06565B.
104. Gonzalez, A., Kengmana, E. S., Fonseca, M. V., Han, G. G. D. (2020). Solid-state photoswitching molecules: Structural design for isomerization in condensed phase. *Materials Today Advances, 6,* 100058. DOI 10.1016/j.mtadv.2020.100058.
105. Qu, L., Xu, X., Song, J., Wu, D., Wang, L. et al. (2020). Solid-state photochromic molecular switches based on axially chiral and helical spiropyrans. *Dyes and Pigments, 181,* 108597. DOI 10.1016/j.dyepig.2020.108597.
106. Lin, S., Gutierrez-Cuevas, K. G., Zhang, X., Guo, J., Li, Q. (2021). Fluorescent photochromic α-cyanodiarylethene molecular switches: An emerging and promising class of functional diarylethene. *Advanced Functional Materials, 31(7),* 2007957. DOI 10.1002/adfm.202007957.
107. Yang, Y., Chen, Y., Li, Y., Wang, Z., Zhao, H. (2022). Acid-, mechano-and photochromic molecular switches based on a spiropyran derivative for rewritable papers. *Materials Chemistry Frontiers, 6(7),* 916–923. DOI 10.1039/D1QM01637G.
108. Rad, J. K., Balzade, Z., Mahdavian, A. R. (2022). Spiropyran-based advanced photoswitchable materials: A fascinating pathway to the future stimuli-responsive devices. *Journal of Photochemistry and Photobiology C: Photochemistry Reviews,* 51*,* 100487.
109. Kajiya, R., Sakakibara, S., Ikawa, H., Higashiguchi, K., Matsuda, K. et al. (2019). Inorganic–organic hybrid photomechanical crystals consisting of diarylethenes and cage siloxanes. *Chemistry of Materials, 31(22),* 9372–9378. DOI 10.1021/acs.chemmater.9b02941.
110. Pizarro, G. D. C., Alavia, W., González, K., Díaz, H., Marambio, O. G. et al. (2022). Design and study of a photo-switchable polymeric system in the presence of ZnS nanoparticles under the influence of UV light irradiation. *Polymers, 14(5),* 945. DOI 10.3390/polym14050945.
111. Kobatake, S., Takami, S., Muto, H., Ishikawa, T., Irie, M. (2007). Rapid and reversible shape changes of molecular crystals on photoirradiation. *Nature, 446(7137),* 778–781. DOI 10.1038/nature05669.
112. Al-Kaysi, R. O., Bardeen, C. J. (2007). Reversible photoinduced shape changes of crystalline organic nanorods. *Advanced Materials, 19(9),* 1276–1280. DOI 10.1002/(ISSN)1521-4095.
113. Terao, F., Morimoto, M., Irie, M. (2012). Light-driven molecular-crystal actuators: Rapid and reversible bending of rodlike mixed crystals of diarylethene derivatives. *Angewandte Chemie International Edition, 51(4),* 901–904. DOI 10.1002/anie.201105585.

114. Zhu, L., Al-Kaysi, R. O., Bardeen, C. J. (2011). Reversible photoinduced twisting of molecular crystal microribbons. *Journal of the American Chemical Society, 133(32),* 12569–12575. DOI 10.1021/ja201925p.
115. Koshima, H., Ojima, N., Uchimoto, H. (2009). Mechanical motion of azobenzene crystals upon photoirradiation. *Journal of the American Chemical Society, 131(20),* 6890–6891. DOI 10.1021/ja8098596.
116. Koshima, H., Takechi, K., Uchimoto, H., Shiro, M., Hashizume, D. (2011). Photomechanical bending of salicylideneaniline crystals. *Chemical Communications, 47(41),* 11423–11425. DOI 10.1039/c1cc14288g.
117. Nakano, H. (2010). Direction control of photomechanical bending of a photochromic molecular fiber. *Journal of Materials Chemistry, 20(11),* 2071–2074. DOI 10.1039/b924718a.
118. Morimoto, M., Irie, M. (2010). A diarylethene cocrystal that converts light into mechanical work. *Journal of the American Chemical Society, 132(40),* 14172–14178. DOI 10.1021/ja105356w.
119. Huang, Y., Yu, Q., Su, C., Jiang, J., Chen, N. et al. (2021). Light-responsive soft actuators: Mechanism, materials, fabrication, and applications. *Actuators, 10(11),* 298. DOI 10.3390/act10110298.
120. Warner, M., Terentjev, E. M. (2007). *Liquid crystal elastomers,* vol. 120. UK: Oxford University Press.
121. Hogan, P. M., Tajbakhsh, A. R., Terentjev, E. M. (2002). UV manipulation of order and macroscopic shape in nematic elastomers. *Physical Review E, 65(4),* 041720. DOI 10.1103/PhysRevE.65.041720.
122. Finkelmann, H., Nishikawa, E., Pereira, G. G., Warner, M. (2001). A new opto-mechanical effect in solids. *Physical Review Letters, 87(1),* 015501. DOI 10.1103/PhysRevLett.87.015501.
123. Barrett, C. J., Mamiya, J. I., Yager, K. G., Ikeda, T. (2007). Photo-mechanical effects in azobenzene-containing soft materials. *Soft Matter, 3(10),* 1249–1261. DOI 10.1039/b705619b.
124. Cai, F., Chen, Y. X., Wang, W. Z., Yu, H. F. (2021). Macroscopic regulation of hierarchical nanostructures in liquid-crystalline block copolymers towards functional materials. *Chinese Journal of Polymer Science, 39(4),* 397–416. DOI 10.1007/s10118-021-2531-1.
125. Eleya, N., Ghosh, S., Lork, E., Staubitz, A. (2021). A new photo switchable azobenzene macrocycle without thermal relaxation at ambient temperature. *Journal of Materials Chemistry C, 9(1),* 82–87. DOI 10.1039/D0TC05211F.
126. Yadavalli, N. S., Loebner, S., Papke, T., Sava, E., Hurduc, N. et al. (2016). A comparative study of photoinduced deformation in azobenzene containing polymer films. *Soft Matter, 12(9),* 2593–2603. DOI 10.1039/C6SM00029K.
127. Nuñez, D. G., Fasce, D., Galante, M. J., Oyanguren, P. A. (2021). Photo-induced changes in azobenzene-containing soft materials. *Optical Materials, 115,* 111032. DOI 10.1016/j.optmat.2021.111032.
128. White, T. J., Tabiryan, N. V., Serak, S. V., Hrozhyk, U. A., Tondiglia, V. P. et al. (2008). A high frequency photodriven polymer oscillator. *Soft Matter, 4(9),* 1796–1798. DOI 10.1039/b805434g.
129. Zhao, D., Liu, Y. (2019). Photomechanical vibration energy harvesting based on liquid crystal elastomer cantilever. *Smart Materials and Structures, 28(7),* 075017. DOI 10.1088/1361-665X/ab15ab.
130. Yue, Y., Norikane, Y., Azumi, R., Koyama, E. (2018). Light-induced mechanical response in crosslinked liquid-crystalline polymers with photoswitchable glass transition temperatures. *Nature Communications, 9(1),* 1–8. DOI 10.1038/s41467-018-05744-x.
131. Gelebart, A. H., Jan Mulder, D., Varga, M., Konya, A., Vantomme, G. et al. (2017). Making waves in a photoactive polymer film. *Nature, 546(7660),* 632–636. DOI 10.1038/nature22987.
132. Li, M., Lv, S., Zhou, J. (2014). Photo-thermo-mechanically actuated bending and snapping kinetics of liquid crystal elastomer cantilever. *Smart Materials and Structures, 23(12),* 125012. DOI 10.1088/0964-1726/23/12/125012.
133. Greco, F., Domenici, V., Desii, A., Sinibaldi, E., Zupančič, B. et al. (2013). Liquid single crystal elastomer/conducting polymer bilayer composite actuator: Modelling and experiments. *Soft Matter, 9(47),* 11405–11416. DOI 10.1039/c3sm51153g.

134. Kuzyk, M. G., Dawson, N. J. (2020). Photomechanical materials and applications: A tutorial. *Advances in Optics and Photonics, 12(4),* 847–1011. DOI 10.1364/AOP.387366.

135. Wie, J. J., Wang, D. H., Tondiglia, V. P., Tabiryan, N. V., Vergara-Toloza, R. O. et al. (2014). Photopiezoelectric composites of azobenzene-functionalized polyimides and polyvinylidene fluoride. *Macromolecular Rapid Communications, 35(24),* 2050–2056. DOI 10.1002/marc.201400455.

136. Tang, R., Liu, Z., Xu, D., Liu, J., Yu, L. et al. (2015). Optical pendulum generator based on photomechanical liquid-crystalline actuators. *ACS Applied Materials & Interfaces, 7(16),* 8393–8397. DOI 10.1021/acsami.5b01732.

137. Lin, W., Pan, M., Xiao, Q., Li, H., Wang, C. (2019). Tuning the capture of CO_2 through entropic effect induced by reversible trans–cis isomerization of light-responsive ionic liquids. *The Journal of Physical Chemistry Letters, 10(12),* 3346–3351. DOI 10.1021/acs.jpclett.9b01023.

138. Yu, Y., Ikeda, T. (2006). Soft actuators based on liquid-crystalline elastomers. *Angewandte Chemie International Edition, 45(33),* 5416–5418. DOI 10.1002/(ISSN)1521-3773.

139. Li, A., Yuan, B., Li, W., Wang, F., Ha, Y. (2013). Thermally induced isomerization of linoleic acid in soybean oil. *Chemistry and Physics of Lipids, 166,* 55–60. DOI 10.1016/j.chemphyslip.2012.12.003.

140. Li, Y., Yu, Y., Luo, Q., He, Y., Tian, Z. et al. (2021). Thermally induced isomerization of linoleic acid and α-Linolenic acid in *Rosa roxburghii* Tratt seed oil. *Food Science & Nutrition, 9(6),* 2843–2852. DOI 10.1002/fsn3.2222.

141. Christy, A. A. (2009). Thermally induced isomerization of trilinolein and trilinoelaidin at 250°C: Analysis of products by gas chromatography and infrared spectroscopy. *Lipids, 44(12),* 1105–1112. DOI 10.1007/s11745-009-3363-x.

142. Goebbert, D. J., Wende, T., Jiang, L., Meijer, G., Sanov, A. et al. (2010). IR spectroscopic characterization of the thermally induced isomerization in carbon disulfide dimer anions. *The Journal of Physical Chemistry Letters, 1(16),* 2465–2469. DOI 10.1021/jz100841e.

143. Schex, R., Schweiggert, F., Wüstenberg, B., Bonrath, W., Schäfer, C. et al. (2020). Kinetic and thermodynamic study of the thermally induced (E/Z)-isomerization of the retro-carotenoid rhodoxanthin. *Journal of Agricultural and Food Chemistry, 68(18),* 5259–5269. DOI 10.1021/acs.jafc.0c00933.

144. Wang, D., Zhao, L., Zhao, H., Wu, J., Wagner, M. et al. (2019). Inducing molecular isomerization assisted by water. *Communications Chemistry, 2(1),* 1–8. DOI 10.1038/s42004-019-0221-5.

145. Honda, M., Sowa, T., Kawashima, Y. (2020). Thermal- and photo-induced isomerization of all-*E*- and *Z*-isomer-rich xanthophylls: Astaxanthin and its structurally-related xanthophylls, adonirubin, and adonixanthin. *European Journal of Lipid Science and Technology, 122(5),* 1900462. DOI 10.1002/ejlt.201900462.

146. Zhang, B., Zhu, T., Ou, M., Rowell, N., Fan, H. et al. (2018). Thermally-induced reversible structural isomerization in colloidal semiconductor CdS magic-size clusters. *Nature Communications, 9(1),* 1–10. DOI 10.1038/s41467-018-04842-0.

147. Zhang, J. Q., Zhang, D. S., Chen, Q. J., Xu, H. B., Kurmoo, M. et al. (2019). Thermally induced *trans*-to-*cis* isomerization and its photoinduced reversal monitored using absorption and luminescence: Cooperative effect of metal coordination and steric substituent. *Chemistry–A European Journal, 25(20),* 5177–5185. DOI 10.1002/chem.201900204.

148. Bujak, K., Orlikowska, H., Małecki, J. G., Schab-Balcerzak, E., Bartkiewicz, S. et al. (2019). Fast dark *cis-trans* isomerization of azopyridine derivatives in comparison to their azobenzene analogues: Experimental and computational study. *Dyes and Pigments, 160,* 654–662. DOI 10.1016/j.dyepig.2018.09.006.

149. Simeth, N. A., Crespi, S., Fagnoni, M., König, B. (2018). Tuning the thermal isomerization of phenylazoindole photoswitches from days to nanoseconds. *Journal of the American Chemical Society, 140(8),* 2940–2946.

150. Garcia-Amorós, J., Díaz-Lobo, M., Nonell, S., Velasco, D. (2012). Fastest thermal isomerization of an azobenzene for nanosecond photoswitching applications under physiological conditions. *Angewandte Chemie, 124(51),* 12992–12995.

151. Poutanen, M., Ahmed, Z., Rautkari, L., Ikkala, O., Priimagi, A. (2018). Thermal isomerization of hydroxyazobenzenes as a platform for vapor sensing. *ACS Macro Letters, 7(3),* 381–386.

152. Huber, L. A., Mayer, P., Dube, H. (2018). Photoisomerization of mono-arylated indigo and water-induced acceleration of thermal cis-to-trans isomerization. *ChemPhotoChem, 2(6),* 458–464.
153. Titov, E., Lysyakova, L., Lomadze, N., Kabashin, A. V., Saalfrank, P. et al. (2015). Thermal cis-to-trans isomerization of azobenzene-containing molecules enhanced by gold nanoparticles: An experimental and theoretical study. *The Journal of Physical Chemistry C, 119(30),* 17369–17377.
154. Wang, Z., Roffey, A., Losantos, R., Lennartson, A., Jevric, M. et al. (2019). Macroscopic heat release in a molecular solar thermal energy storage system. *Energy & Environmental Science, 12(1),* 187–193.
155. Waidhas, F., Jevric, M., Bosch, M., Yang, T., Franz, E. et al. (2020). Electrochemically controlled energy release from a norbornadiene-based solar thermal fuel: Increasing the reversibility to 99.8% using HOPG as the electrode material. *Journal of Materials Chemistry A, 8(31),* 15658–15664.
156. Wang, Z., Moïse, H., Cacciarini, M., Nielsen, M. B., Morikawa, M. A. et al. (2021). Liquid-based multijunction molecular solar thermal energy collection device. *Advanced Science, 8(21),* 2103060.
157. Wang, Z., Wu, Z., Hu, Z., Orrego-Hernández, J., Mu, E. et al. (2022). Chip-scale solar thermal electrical power generation. *Cell Reports Physical Science, 3(3),* 100789.
158. Bönisch, M., Panigrahi, A., Stoica, M., Calin, M., Ahrens, E. et al. (2017). Giant thermal expansion and α-precipitation pathways in Ti-alloys. *Nature Communications, 8(1),* 1–9.
159. Saharan, L., Tadesse, Y. (2019). Novel twisted and coiled polymer artificial muscles for biomedical and robotics applications. In: *Materials for biomedical engineering*, pp. 45–75. Amsterdam: Elsevier.
160. Zhang, J., Sheng, J., O'Neill, C. T., Walsh, C. J., Wood, R. J. et al. (2019). Robotic artificial muscles: Current progress and future perspectives. *IEEE Transactions on Robotics, 35(3),* 761–781. DOI 10.1109/TRO.8860.
161. Bhatti, M. R. A., Bilotti, E., Zhang, H., Varghese, S., Verpaalen, R. C. et al. (2020). Ultra-high actuation stress polymer actuators as light-driven artificial muscles. *ACS Applied Materials Interfaces, 12(29),* 33210–33218. DOI 10.1021/acsami.0c07684.
162. Mamiya, J. I. (2013). Photomechanical energy conversion based on cross-linked liquid-crystalline polymers. *Polymer Journal, 45(3),* 239–246. DOI 10.1038/pj.2012.140.
163. Cherubini, A., Moretti, G., Vertechy, R., Fontana, M. (2015). Experimental characterization of thermally-activated artificial muscles based on coiled nylon fishing lines. *AIP Advances, 5(6),* 067158. DOI 10.1063/1.4923315.
164. Haines, C. S., Lima, M. D., Li, N., Spinks, G. M., Foroughi, J. et al. (2014). Artificial muscles from fishing line and sewing thread. *Science, 343(6173),* 868–872. DOI 10.1126/science.1246906.
165. Chou, C. E., Liu, Y. L., Zhang, Y., Hsueh, C. H., Yang, F. et al. (2020). Thermomechanical deformation of polyethylene-terephthalate artificial muscles. *Polymer, 210,* 123013. DOI 10.1016/j.polymer.2020.123013.
166. Liu, C., Qin, H., Mather, P. T. (2007). Review of progress in shape-memory polymers. *Journal of Materials Chemistry, 17(16),* 1543–1558. DOI 10.1039/b615954k.
167. Xu, L., Peng, Q., Zhao, X., Li, P., Xu, J. et al. (2020). A photoactuator based on stiffness-variable carbon nanotube nanocomposite yarn. *ACS Applied Materials & Interfaces, 12(36),* 40711–40718. DOI 10.1021/acsami.0c14222.
168. Govorov, A. O., Zhang, W., Skeini, T., Richardson, H., Lee, J. et al. (2006). Gold nanoparticle ensembles as heaters and actuators: Melting and collective plasmon resonances. *Nanoscale Research Letters, 1(1),* 84–90. DOI 10.1007/s11671-006-9015-7.
169. Cresta, V., Romano, G., Kolpak, A., Zalar, B., Domenici, V. (2018). Nanostructured composites based on liquid-crystalline elastomers. *Polymers, 10(7),* 773. DOI 10.3390/polym10070773.
170. Schmidt, A. M. (2006). Electromagnetic activation of shape memory polymer networks containing magnetic nanoparticles. *Macromolecular Rapid Communications, 27(14),* 1168–1172. DOI 10.1002/(ISSN)1521-3927.
171. Jia, H., Gu, S. Y. (2020). A near infrared induced self-healable composite based on disulfide bonds for flexible electronics. *Journal of Polymer Research, 27(10),* 1–13. DOI 10.1007/s10965-020-02186-2.

172. Dai, S., Zhou, X., Hu, X., Dong, X., Jiang, Y. et al. (2021). Carbon nanotube hybrid yarn with mechanically strong healable silicone elastomers for artificial muscle. *ACS Applied Nano Materials, 4(5),* 5123–5130. DOI 10.1021/acsanm.1c00576.

173. Feng, H., Tang, N., An, M., Guo, R., Ma, D. et al. (2019). Thermally-responsive hydrogels poly(N-isopropylacrylamide) as the thermal switch. *The Journal of Physical Chemistry C, 123(51),* 31003–31010. DOI 10.1021/acs.jpcc.9b08594.

174. Liu, Z., Gao, Q., Chen, J., Deng, J., Lin, K. et al. (2018). Negative thermal expansion in molecular materials. *Chemical Communications, 54(41),* 5164–5176. DOI 10.1039/C8CC01153B.

175. Hu, Y., Chen, J., Wang, B. (2015). On the intrinsic ripples and negative thermal expansion of graphene. *Carbon, 95,* 239–249. DOI 10.1016/j.carbon.2015.08.022.

176. Yoon, D., Son, Y. W., Cheong, H. (2011). Negative thermal expansion coefficient of graphene measured by Raman spectroscopy. *Nano Letters, 11(8),* 3227–3231. DOI 10.1021/nl201488g.

177. Brooker, S. (2015). Spin crossover with thermal hysteresis: Practicalities and lessons learnt. *Chemical Society Reviews, 44(10),* 2880–2892. DOI 10.1039/C4CS00376D.

178. Mullaney, B. R., Goux-Capes, L., Price, D. J., Chastanet, G., Létard, J. F. et al. (2017). Spin crossover-induced colossal positive and negative thermal expansion in a nanoporous coordination framework material. *Nature Communications, 8(1),* 1–6. DOI 10.1038/s41467-017-00776-1.

179. Jones, R. H., Knight, K. S., Marshall, W. G., Clews, J., Darton, R. J. et al. (2014). Colossal thermal expansion and negative thermal expansion in simple halogen bonded complexes. *CrystEngComm, 16(2),* 237–243. DOI 10.1039/C3CE41909F.

180. Hutchins, K. M., Unruh, D. K., Carpenter, D. D., Groeneman, R. H. (2018). Thermal expansion along one-dimensional chains and two-dimensional sheets within co-crystals based on halogen or hydrogen bonds. *CrystEngComm, 20(45),* 7232–7235. DOI 10.1039/C8CE01090K.

181. Das, D., Jacobs, T., Barbour, L. J. (2010). Exceptionally large positive and negative anisotropic thermal expansion of an organic crystalline material. *Nature Materials, 9(1),* 36–39. DOI 10.1038/nmat2583.

182. Kim, H. S., Choi, S. M., Pate, B. D., Kang, S. H., Sim, J. B. et al. (2015). Negative and positive anisotropic thermal expansions in a hexagonally packed columnar discotic liquid crystal thin film. *Chemistry of Materials, 27(9),* 3417–3421. DOI 10.1021/acs.chemmater.5b00720.

183. Kimura, D., Irisawa, T., Takagi, K., Tahara, K., Sakurai, D. et al. (2021). Mechanism for anisotropic thermal expansion of polyamide fibers. *Sensors and Actuators B: Chemical, 344,* 130262. DOI 10.1016/j.snb.2021.130262.

184. Wu, C., Zhou, S. (1995). Laser light scattering study of the phase transition of poly(N-isopropylacrylamide) in water. 1. Single chain. *Macromolecules, 28(24),* 8381–8387. DOI 10.1021/ma00128a056.

185. Sun, Q., Jin, K., Huang, Y., Guo, J., Rungrotmongkol, T. et al. (2021). Influence of conformational change of chain unit on the intrinsic negative thermal expansion of polymers. *Chinese Chemical Letters, 32(4),* 1515–1518. DOI 10.1016/j.cclet.2020.09.046.

186. Shen, X., Viney, C., Johnson, E. R., Wang, C., Lu, J. Q. (2013). Large negative thermal expansion of a polymer driven by a submolecular conformational change. *Nature Chemistry, 5(12),* 1035–1041. DOI 10.1038/nchem.1780.

187. Shen, X., Connolly, T., Huang, Y., Colvin, M., Wang, C. et al. (2016). Adjusting local molecular environment for giant ambient thermal contraction. *Macromolecular Rapid Communications, 37(23),* 1904–1911. DOI 10.1002/marc.201600045.

188. Gao, D., Lin, M. F., Xiong, J., Li, S., Lou, S. N. et al. (2020). Photothermal actuated origamis based on graphene oxide–cellulose programmable bilayers. *Nanoscale Horizons, 5(4),* 730–738. DOI 10.1039/C9NH00719A.

189. Poppinga, S., Zollfrank, C., Prucker, O., Rühe, J., Menges, A. et al. (2018). Toward a new generation of smart biomimetic actuators for architecture. *Advanced Materials, 30(19),* 1703653. DOI 10.1002/adma.201703653.

190. Li, C., Liu, Y., Huang, X., Jiang, H. (2012). Direct sun-driven artificial heliotropism for solar energy harvesting based on a photo-thermomechanical liquid-crystal elastomer nanocomposite. *Advanced Functional Materials, 22(24),* 5166–5174. DOI 10.1002/adfm.201202038.

191. Deng, J., Li, J., Chen, P., Fang, X., Sun, X. et al. (2016). Tunable photothermal actuators based on a pre-programmed aligned nanostructure. *Journal of the American Chemical Society, 138(1),* 225–230. DOI 10.1021/jacs.5b10131.

192. Wani, O. M., Zeng, H., Priimagi, A. (2017). A light-driven artificial flytrap. *Nature Communications, 8(1),* 1–7. DOI 10.1038/ncomms15546.

193. Faccenda, M., Dal Zilio, L. (2017). The role of solid–solid phase transitions in mantle convection. *Lithos, 268,* 198–224. DOI 10.1016/j.lithos.2016.11.007.

194. Bailey, J. B., Tezcan, F. A. (2020). Tunable and cooperative thermomechanical properties of protein–metal–organic frameworks. *Journal of the American Chemical Society, 142(41),* 17265–17270. DOI 10.1021/jacs.0c07835.

195. Maspoch, D., Ruiz-Molina, D., Wurst, K., Domingo, N., Cavallini, M. et al. (2003). A nanoporous molecular magnet with reversible solvent-induced mechanical and magnetic properties. *Nature Materials, 2(3),* 190–195. DOI 10.1038/nmat834.

196. Smets, M. M. H., Kalkman, E., Krieger, A., Tinnemans, P., Meekes, H. et al. (2020). On the mechanism of solid-state phase transitions in molecular crystals–the role of cooperative motion in (quasi)racemic linear amino acids. *IUCrJ, 7(2),* 331–341. DOI 10.1107/S2052252520001335.

197. Zhu, S., Wu, P., Yelemulati, H., Hu, J., Li, G. et al. (2021). Anomalous thermally expanded polymer networks for flexible perceptual devices. *Matter, 4(6),* 1832–1862. DOI 10.1016/j.matt.2021.03.010.

198. Zhou, H. L., Zhang, Y. B., Zhang, J. P., Chen, X. M. (2015). Supramolecular-jack-like guest in ultramicroporous crystal for exceptional thermal expansion behaviour. *Nature Communications, 6(1),* 6917. DOI 10.1038/ncomms7917.

199. Scherb, S., Hinaut, A., Pawlak, R., Vilhena, J. G., Liu, Y. et al. (2020). Giant thermal expansion of a two-dimensional supramolecular network triggered by alkyl chain motion. *Communications Materials, 1(1),* 8. DOI 10.1038/s43246-020-0009-2.

200. Kim, Y. S., Liu, M., Ishida, Y., Ebina, Y., Osada, M. et al. (2015). Thermoresponsive actuation enabled by permittivity switching in an electrostatically anisotropic hydrogel. *Nature Materials, 14(10),* 1002–1007. DOI 10.1038/nmat4363.

201. Wight, C. D., Xiao, Q., Wagner, H. R., Hernandez, E. A., Lynch, V. M. et al. (2020). Mechanistic analysis of solid-state colorimetric switching: Monoalkoxynaphthalene-naphthalimide donor–acceptor dyads. *Journal of the American Chemical Society, 142(41),* 17630–17643. DOI 10.1021/jacs.0c08137.

202. Zhang, X., Hu, M., Poulikakos, D. (2012). A Low-frequency wave motion mechanism enables efficient energy transport in carbon nanotubes at high heat fluxes. *Nano Letters, 12(7),* 3410–3416. DOI 10.1021/nl300261r.

203. Yao, W. J., Cao, B. Y. (2016). Triggering wave-domain heat conduction in graphene. *Physics Letters A, 380(24),* 2105–2110. DOI 10.1016/j.physleta.2016.04.024.

204. Chen, X. K., Liu, J., Peng, Z. H., Du, D., Chen, K. Q. (2017). A Wave-dominated heat transport mechanism for negative differential thermal resistance in graphene/hexagonal boron nitride heterostructures. *Applied Physics Letters, 110(9),* 091907. DOI 10.1063/1.4977776.

205. Liu, B., Baimova, J. A., Reddy, C. D., Dmitriev, S. V., Law, W. K. et al. (2014). Interface thermal conductance and rectification in hybrid graphene/silicene monolayer. *Carbon, 79,* 236–244. DOI 10.1016/j.carbon.2014.07.064.

206. Liu, Y. Y., Zhou, W. X., Tang, L. M., Chen, K. Q. (2014). An important mechanism for thermal rectification in graded nanowires. *Applied Physics Letters, 105(20),* 203111. DOI 10.1063/1.4902427.

207. Zheng, K., Wang, L., Bai, S., Yu, J., Tang, Z. et al. (2014). An anomalous wave-like kinetic energy transport in graphene nanoribbons at high heat flux. *Physica B: Condensed Matter, 434,* 64–68. DOI 10.1016/j.physb.2013.10.050.

208. Zheng, X. Q., Lee, J., Feng, P. X. L. (2017). Hexagonal boron nitride nanomechanical resonators with spatially visualized motion. *Microsystems & Nanoengineering, 3(1),* 17038. DOI 10.1038/micronano.2017.38.

209. Shiri, D., Isacsson, A. (2019). Heat-to-mechanical energy conversion in graphene: Manifestation of Umklapp enhancement with strain. *Journal of Applied Physics, 125(12),* 125101. DOI 10.1063/1.5081902.

210. Tian, H., Li, C., Mohammad, M. A., Cui, Y. L., Mi, W. T. et al. (2014). Graphene earphones: Entertainment for both humans and animals. *ACS Nano, 8(6),* 5883–5890. DOI 10.1021/nn5009353.
211. Ghasemi Yeklangi, A., Khadem, S. E., Darbari, S. (2018). Fabrication and investigation of a thermoacoustic loudspeaker based on carbon nanotube coated laser-scribed graphene. *Journal of Applied Physics, 124(22),* 224501. DOI 10.1063/1.5038729.
212. Tu, T., Ju, Z. Y., Li, Y. T., Gou, G. Y., Tian, Y. et al. (2019). A novel thermal acoustic device based on vertical graphene film. *AIP Advances, 9(7),* 075302. DOI 10.1063/1.5096220.
213. Dong, Q., Bae, H., Zhang, Z., Chen, Y., Wen, Z. et al. (2019). Miniature fiber optic acoustic pressure sensors with air-backed graphene diaphragms. *Journal of Vibration and Acoustics, 141(4),* 041003. DOI 10.1115/1.4042929.
214. Giorgianni, F., Vicario, C., Shalaby, M., Tenuzzo, L. D., Marcelli, A. et al. (2018). High-efficiency and low distortion photoacoustic effect in 3D graphene sponge. *Advanced Functional Materials, 28(2),* 1702652. DOI 10.1002/adfm.201702652.
215. Carvalho, A. F., Kulyk, B., Fernandes, A. J., Fortunato, E., Costa, F. M. (2022). A review on the applications of graphene in mechanical transduction. *Advanced Materials, 34(8),* 2101326. DOI 10.1002/adma.202101326.
216. Lalwani, G., Cai, X., Nie, L., Wang, L. V., Sitharaman, B. (2013). Graphene-based contrast agents for photoacoustic and thermoacoustic tomography. *Photoacoustics, 1(3–4),* 62–67. DOI 10.1016/j.pacs.2013.10.001.
217. Moon, H., Kumar, D., Kim, H., Sim, C., Chang, J. H. et al. (2015). Amplified photoacoustic performance and enhanced photothermal stability of reduced graphene oxide coated gold nanorods for sensitive photoacoustic imaging. *ACS Nano, 9(3),* 2711–2719. DOI 10.1021/nn506516p.
218. Yu, P., Besteiro, L. V., Huang, Y., Wu, J., Fu, L. et al. (2019). Broadband metamaterial absorbers. *Advanced Optical Materials, 7(3),* 1800995. DOI 10.1002/adom.201800995.
219. Zhang, Y., Li, Y., Cao, Y., Liu, Y., Zhang, H. (2017). Graphene induced tunable and polarization-insensitive broadband metamaterial absorber. *Optics Communications, 382,* 281–287. DOI 10.1016/j.optcom.2016.08.003.
220. Zhu, X., Shi, L., Schmidt, M. S., Boisen, A., Hansen, O. et al. (2013). Enhanced light–matter interactions in graphene-covered gold nanovoid arrays. *Nano Letters, 13(10),* 4690–4696. DOI 10.1021/nl402120t.
221. Konstantatos, G., Badioli, M., Gaudreau, L., Osmond, J., Bernechea, M. et al. (2012). Hybrid graphene–quantum dot phototransistors with ultrahigh gain. *Nature Nanotechnology, 7(6),* 363–368. DOI 10.1038/nnano.2012.60.
222. Wang, Z., Li, T., Almdal, K., Mortensen, N. A., Xiao, S. et al. (2016). Experimental demonstration of graphene plasmons working close to the near-infrared window. *Optics Letters, 41(22),* 5345–5348. DOI 10.1364/OL.41.005345.
223. Jia, X., Wang, X., Yuan, C., Meng, Q., Zhou, Z. (2016). Novel dynamic tuning of broadband visible metamaterial perfect absorber using graphene. *Journal of Applied Physics, 120(3),* 033101. DOI 10.1063/1.4956437.
224. Zhu, H., Yi, F., Cubukcu, E. (2016). Plasmonic metamaterial absorber for broadband manipulation of mechanical resonances. *Nature Photonics, 10(11),* 709–714. DOI 10.1038/nphoton.2016.183.
225. Zou, Y., Cao, J., Gong, X., Qian, R., An, Z. (2019). Ultrathin and electrically tunable metamaterial with nearly perfect absorption in mid-infrared. *Applied Sciences, 9(16),* 3358. DOI 10.3390/app9163358.
226. Ou, J. Y., Plum, E., Jiang, L., Zheludev, N. I. (2011). Reconfigurable photonic metamaterials. *Nano Letters, 11(5),* 2142–2144. DOI 10.1021/nl200791r.
227. Lee, S., Seo, M. K. (2021). Full three-dimensional wavelength-scale plasmomechanical resonator. *Optics Letters, 46(6),* 1317–1320. DOI 10.1364/OL.416695.
228. Maurer, T., Marae-Djouda, J., Cataldi, U., Gontier, A., Montay, G. et al. (2015). The beginnings of plasmomechanics: Towards plasmonic strain sensors. *Frontiers of Materials Science, 9(2),* 170–177. DOI 10.1007/s11706-015-0290-z.
229. Roxworthy, B. J., Aksyuk, V. A. (2016). Nanomechanical motion transduction with a scalable localized gap plasmon architecture. *Nature Communications, 7(1),* 13746. DOI 10.1038/ncomms13746.

230. Caputo, R., Cataldi, U., Bürgi, T., Umeton, C. (2015). Plasmomechanics: A colour-changing device based on the plasmonic coupling of gold nanoparticles. *Molecular Crystals and Liquid Crystals, 614(1),* 20–29. DOI 10.1080/15421406.2015.1049897.

231. Koya, A. N., Cunha, J., Guerrero-Becerra, K. A., Garoli, D., Wang, T. et al. (2021). Plasmomechanical systems: Principles and applications. *Advanced Functional Materials, 31(41),* 2103706. DOI 10.1002/adfm.202103706.

232. Bradshaw, D. S., Andrews, D. L. (2017). Manipulating particles with light: Radiation and gradient forces. *European Journal of Physics, 38(3),* 034008. DOI 10.1088/1361-6404/aa6050.

233. Raziman, T. V., Wolke, R. J., Martin, O. J. (2015). Optical forces in nanoplasmonic systems: How do they work, what can they be useful for? *Faraday Discussions, 178,* 421–434. DOI 10.1039/C4FD00224E.

234. Ginis, V., Tassin, P., Soukoulis, C. M., Veretennicoff, I. (2013). Enhancing optical gradient forces with metamaterials. *Physical Review Letters, 110(5),* 057401. DOI 10.1103/PhysRevLett.110.057401.

235. Hogan, N. J., Urban, A. S., Ayala-Orozco, C., Pimpinelli, A., Nordlander, P. et al. (2014). Nanoparticles heat through light localization. *Nano Letters, 14(8),* 4640–4645. DOI 10.1021/nl5016975.

236. Thijssen, R., Kippenberg, T. J., Polman, A., Verhagen, E. (2015). Plasmomechanical resonators based on dimer nanoantennas. *Nano Letters, 15(6),* 3971–3976. DOI 10.1021/acs.nanolett.5b00858.

237. Kosaka, P. M., Pini, V., Ruz, J. J., Da Silva, R. A., González, M. U. et al. (2014). Detection of cancer biomarkers in serum using a hybrid mechanical and optoplasmonic nanosensor. *Nature Nanotechnology, 9(12),* 1047–1053. DOI 10.1038/nnano.2014.250.

238. Hu, H., Zhang, S., Xu, H. (2019). Closely packed metallic nanocuboid dimer allowing plasmomechanical strong coupling. *Physical Review A, 99(3),* 033815. DOI 10.1103/PhysRevA.99.033815.

239. Roxworthy, B. J., Vangara, S., Aksyuk, V. A. (2018). Subdiffraction spatial mapping of nanomechanical modes using a plasmomechanical system. *ACS Photonics, 5(9),* 3658–3665. DOI 10.1021/acsphotonics.8b00604.

240. Kassem, S., van Leeuwen, T., Lubbe, A. S., Wilson, M. R., Feringa, B. L. et al. (2017). Artificial molecular motors. *Chemical Society Reviews, 46(9),* 2592–2621. DOI 10.1039/C7CS00245A.

241. Groppi, J., Baroncini, M., Venturi, M., Silvi, S., Credi, A. (2019). Design of photo-activated molecular machines: Highlights from the past ten years. *Chemical Communications, 55(84),* 12595–12602. DOI 10.1039/C9CC06516D.

242. Balzani, V., Credi, A., Venturi, M. (2008). *Molecular devices and machines: Concepts and perspectives for the nanoworld*, pp. 69–106. Weinheim: John Wiley & Sons.

243. Dattler, D., Fuks, G., Heiser, J., Moulin, E., Perrot, A. et al. (2019). Design of collective motions from synthetic molecular switches, rotors, and motors. *Chemical Reviews, 120(1),* 310–433. DOI 10.1021/acs.chemrev.9b00288.

244. Astumian, R. D. (2017). How molecular motors work–insights from the molecular machinist's toolbox: The nobel prize in Chemistry 2016. *Chemical Science, 8(2),* 840–845. DOI 10.1039/C6SC04806D.

245. Nakano, H., Suzuki, M. (2012). Photoinduced mass flow of photochromic molecular materials. *Journal of Materials Chemistry, 22(9),* 3702–3704. DOI 10.1039/c2jm16517a.

246. Roke, D., Wezenberg, S. J., Feringa, B. L. (2018). Molecular rotary motors: Unidirectional motion around double bonds. *Proceedings of the National Academy of Sciences, 115(38),* 9423–9431. DOI 10.1073/pnas.1712784115.

247. Filatov, M., Paolino, M., Min, S. K., Kim, K. S. (2018). Fulgides as light-driven molecular rotary motors: Computational design of a prototype compound. *The Journal of Physical Chemistry Letters, 9(17),* 4995–5001. DOI 10.1021/acs.jpclett.8b02268.

248. van Leeuwen, T., Danowski, W., Pizzolato, S. F., Štacko, P., Wezenberg, S. J. et al. (2018). Braking of a light-driven molecular rotary motor by chemical stimuli. *Chemistry–A European Journal, 24(1),* 81–84. DOI 10.1002/chem.201704747.

249. Hou, J., Mondal, A., Long, G., de Haan, L., Zhao, W. et al. (2021). Photo-responsive helical motion by light-driven molecular motors in a liquid-crystal network. *Angewandte Chemie International Edition, 60(15),* 8251–8257. DOI 10.1002/anie.202016254.

250. Berrocal, J. A., Pfeifer, L., Heijnen, D., Feringa, B. L. (2020). Synthesis of core-modified third-generation light-driven molecular motors. *The Journal of Organic Chemistry, 85(16),* 10670–10680. DOI 10.1021/acs.joc.0c01235.

251. Kistemaker, J. C., Štacko, P., Roke, D., Wolters, A. T., Heideman, G. H. et al. (2017). Third-generation light-driven symmetric molecular motors. *Journal of the American Chemical Society, 139(28),* 9650–9661. DOI 10.1021/jacs.7b04412.

252. Kudernac, T., Ruangsupapichat, N., Parschau, M., Maciá, B., Katsonis, N. et al. (2011). Electrically driven directional motion of a four-wheeled molecule on a metal surface. *Nature, 479(7372),* 208–211. DOI 10.1038/nature10587.

253. Maeda, S., Hara, Y., Sakai, T., Yoshida, R., Hashimoto, S. (2007). Self-walking gel. *Advanced Materials, 19(21),* 3480–3484. DOI 10.1002/(ISSN)1521-4095.

254. Kohlmeyer, R. R., Chen, J. (2013). Wavelength-selective, IR light-driven hinges based on liquid crystalline elastomer composites. *Angewandte Chemie, 125(35),* 9404–9407. DOI 10.1002/ange.201210232.

255. Cheng, H., Zhao, F., Xue, J., Shi, G., Jiang, L. et al. (2016). One single graphene oxide film for responsive actuation. *ACS Nano, 10(10),* 9529–9535. DOI 10.1021/acsnano.6b04769.

256. Sarkisov, S. S., Curley, M. J., Fields, A., Sarkisov, S. S., Adamovsky, G. (2004). Photomechanical effect in films of polyvinylidene fluoride. *Applied Physics Letters, 85(14),* 2747–2749. DOI 10.1063/1.1802390.

257. Sarkisov, S. S., Curley, M. J., Huey, L., Fields, A. B., Sarkisov, S. S., II et al. (2006). Light-driven actuators based on polymer films. *Optical Engineering, 45(3),* 034302. DOI 10.1117/1.2185093.

258. Bull, S. R. (2001). Renewable energy today and tomorrow. *Proceedings of the IEEE, 89(8),* 1216–1226. DOI 10.1109/5.940290.

259. Kishore, R. A., Priya, S. (2018). A review on low-grade thermal energy harvesting: Materials, methods and devices. *Materials*, *11(8)*, 1433. DOI 10.3390/ma11081433.

260. Allain, R. (2020). How much energy can you store in a rubber band? https://www.wired.com/story/how-much-energy-can-you-store-in-a-rubber-band/.